



Multi-Observatory Research of Young Stellar Energetic Flares (MORYSEF): X-Ray-flare-related Phenomena and Multi-epoch Behavior

Konstantin V. Getman¹ , Eric D. Feigelson¹ , Abygail R. Waggoner² , L. Ilsedore Cleeves² , Jan Forbrich³ , Joe P. Ninan⁴ , Oleg Kochukhov⁵ , Vladimir S. Airapetian^{6,7} , Sergio A. Dzib⁸ , Charles J. Law^{2,11} , and Christian Rab^{9,10}

¹ Department of Astronomy & Astrophysics, Pennsylvania State University, 525 Davey Laboratory, University Park, PA 16802, USA; kug1@psu.edu

² University of Virginia, Charlottesville, VA 22904, USA

³ Centre for Astrophysics Research, University of Hertfordshire, College Lane, Hatfield, AL10 9AB, UK

⁴ Department of Astronomy and Astrophysics, Tata Institute of Fundamental Research, Homi Bhabha Road, Colaba, Mumbai 400005, India

⁵ Department of Physics and Astronomy, Uppsala University, Box 516, 75120 Uppsala, Sweden

⁶ American University, 4400 Massachusetts Avenue NW, Washington, DC 20016, USA

⁷ NASA/GSFC/SEEC, Greenbelt, MD 20771, USA

⁸ Max-Planck-Institut für Radioastronomie (MPIfR), Auf dem Hugel 69, 53121 Bonn, Germany

⁹ University Observatory, Faculty of Physics, Ludwig-Maximilians-Universität München, Scheinerstr. 1, D-81679 Munich, Germany

¹⁰ Max-Planck-Institut für extraterrestrische Physik, Giessenbachstrasse 1, D-85748 Garching, Germany

Received 2024 May 31; revised 2024 October 4; accepted 2024 October 6; published 2024 November 22

Abstract

The most powerful stellar flares driven by magnetic energy occur during the early pre-main-sequence (PMS) phase. The Orion Nebula represents the nearest region populated by young stars, showing the greatest number of flares accessible to a single pointing of Chandra. This study is part of a multi-observatory project to explore stellar surface magnetic fields (with the Hobby–Eberly Telescope Habitable-zone Planet Finder, HET-HPF), particle ejections (with the Very Long Baseline Array, VLBA), and disk ionization (with the Atacama Large Millimeter/submillimeter Array, ALMA) immediately following the detection of PMS superflares with Chandra. In 2023 December, we successfully conducted such a multi-telescope campaign. Additionally, by analyzing Chandra data from 2003, 2012, and 2016, we examine the multi-epoch behavior of PMS X-ray emission related to PMS magnetic cyclic activity and ubiquitous versus sample-confined megaflaring. Our findings are as follows. (1) We report detailed stellar quiescent and flare X-ray properties for numerous HET/ALMA/VLBA targets, facilitating ongoing multiwavelength analyses. (2) For numerous moderately energetic flares, we report correlations (or lack thereof) between flare energies and stellar mass/size (presence/absence of disks) for the first time. The former is attributed to the correlation between convection-driven dynamo and stellar volume, while the latter suggests the operation of solar-type flare mechanisms in PMS stars. (3) We find that most PMS stars exhibit minor long-term baseline variations, indicating the absence of intrinsic magnetic dynamo cycles or observational mitigation of cycles by saturated PMS X-rays. (4) We conclude that X-ray megaflares are ubiquitous phenomena in PMS stars, which suggests that all protoplanetary disks and nascent planets are subject to violent high-energy emission and particle irradiation events.

Unified Astronomy Thesaurus concepts: Pre-main sequence stars (1290); X-ray stars (1823); Stellar magnetic fields (1610); Stellar x-ray flares (1637); Stellar flares (1603); Protoplanetary disks (1300)

Materials only available in the online version of record: figure set, machine-readable tables

1. Introduction

1.1. Pre-main-sequence Stellar X-Ray Emission

During the early phase of the stellar evolution, fully convective and fast-rotating pre-main-sequence (PMS) stars continue their descent along the Hayashi tracks on the Hertzsprung–Russell diagram, driven by gravitational contraction (e.g., K. V. Getman et al. 2022). Many PMS stars in the first 1–5 Myr of their life are surrounded by protoplanetary disks (e.g., A. J. W. Richert et al. 2018).

The time-averaged X-ray luminosity of a solar-mass PMS star is 10^3 – 10^4 times that of the present-day Sun (T. Preibisch et al. 2005). High X-ray fluxes from a young Sun can be

attributed to a convection-driven magnetic dynamo within the large convective PMS stellar interior, which is more efficient at generating strong magnetic fields than the tachoclinical dynamo operating in main-sequence stars. The PMS dynamo generates increased magnetic fluxes, producing larger starspots, associated active regions, and X-ray-emitting coronae (e.g., M. K. Browning 2008; U. R. Christensen et al. 2009; K. V. Getman et al. 2023). Observed typical magnetic field strengths in active regions (B_{spot}) of PMS stars are often comparable to those of the current Sun, ranging from 1 to 5 kG (K. R. Sokal et al. 2020). However, the surface filling factors of these regions in PMS stars can exceed 80%, in contrast to less than 10% on the Sun (O. Kochukhov et al. 2020).

The bulk of the observed PMS coronal X-ray emission has two components: (1) quasi-continuous baseline emission (also known as “quiescent” or “characteristic” emission), likely arising from numerous small, unresolved X-ray flares (S. J. Wolk et al. 2005), and (2) episodic large flares. Astrophysical modeling of the X-ray time–energy evolution of large flares from PMS stars,

¹¹ NASA Hubble Fellowship Program Sagan Fellow.



with and without disks, shows that many are driven by magnetic reconnection associated with gigantic magnetic coronal loops reaching altitudes of $(1\text{--}10)R_*$ (F. Favata et al. 2005; K. V. Getman et al. 2008b). The time-averaged X-ray fluxes from young ($t < 5$ Myr) PMS stars saturate with stellar rotation and age, possibly due to the high fractional coverage of surface magnetic active regions and/or associated extensive X-ray coronal structures (T. Preibisch et al. 2005; K. V. Getman et al. 2022).

Studies utilizing X-ray data from the Chandra Orion Ultradeep Project (COUP; K. V. Getman et al. 2005b) have examined the frequency and energetics of large PMS flares in the nearby ($d \sim 400$ pc) Orion Nebula (S. J. Wolk et al. 2005; M. Caramazza et al. 2007; J. F. Colombo et al. 2007). XMM data (B. Stelzer et al. 2007) have been employed for the Taurus Molecular Cloud region ($d \sim 140$ pc). More recently, Chandra data have been used to investigate 40 more distant ($1 \text{ kpc} < d < 3 \text{ kpc}$) and rich star-forming regions (K. V. Getman & E. D. Feigelson 2021). These studies consistently show that the energy distribution of large PMS flares ($dN/dE_X \sim E_X^{-\alpha}$) follows a power law with a slope of $\alpha \sim 2$ similar to what is observed in older stars and the contemporary Sun. However, in stark contrast to the Sun, solar-mass PMS stars exhibit flares that are millions of times more powerful and occur at a rate over a million times higher. The contemporary Sun is likely incapable of producing X-ray superflares ($E_X > 10^{34}$ erg) and megaflares ($E_X > 10^{36}$ erg) that frequently occur in PMS stars (K. V. Getman & E. D. Feigelson 2021).

Our current study is part of a multiwavelength, multi-observatory project titled the Multi-Observatory Research of Young Stellar Energetic Flares (MORYSEF), aimed at investigating various aspects of PMS X-ray emission. These aspects include (1) assessing the strength of PMS surface magnetic fields following a large X-ray flare, (2) investigating the effects of X-ray flares on disks' chemistry, (3) searching for flare-associated coronal mass ejections (CMEs), and (4) examining the multi-epoch behaviors of both characteristic and flare X-ray emission.

To address aspects 1, 2, and 3, in 2023 December we initiated nearly simultaneous observations using the Chandra X-ray telescope, the Habitable-zone Planet Finder (HPF) near-infrared (NIR) instrument on the Hobby–Eberly Telescope (HET), the Atacama Large Millimeter/submillimeter Array (ALMA), and the Very Long Baseline Array (VLBA), focusing on young stars in the Orion Nebula star-forming region. Chandra's field of view encompasses large parts of the Orion Nebula Cluster (ONC) and the underlying Orion Molecular Cloud 1 (OMC-1). To address aspect 4, in addition to the X-ray observations in 2023, we reanalyzed earlier Chandra observations from 2003 (COUP observations), 2012, and 2016 of the same region.

1.2. Scientific Objectives of Our Multi-telescope Campaign

Assessing the strength of PMS surface magnetic fields following a large X-ray flare. For normal stars, including main-sequence and PMS stars, a simple power-law relationship has been established between X-ray luminosity and the integrated magnetic flux $\Phi = B \times A$, where B is the surface magnetic field and A is the surface area involved (A. A. Pevtsov et al. 2003; A. S. Kirichenko & S. A. Bogachev 2017; K. V. Getman et al. 2023). This relationship, $L_X \propto \Phi^m$ with $m = 1.0\text{--}1.5$, holds over 12 orders of magnitude from the smallest solar magnetic structures to the continuous emission

from PMS stars (Figure 8 in K. V. Getman et al. 2021). This relationship appears to indicate the universality of the propagation of magnetic flux from the stellar interior to the stellar surface, regardless of the nature of the underlying magnetic dynamo—whether convection driven in PMS stars or tachocline driven in the current old Sun.

However, a major discrepancy is seen with most powerful PMS super- and megaflares with X-ray energies $E_X > 10^{35}$ erg (Figure 8 in K. V. Getman et al. 2021). Assuming equipartition of magnetic fields in modeled X-ray flaring coronal loops, the L_X values are $10^3\text{--}10^4$ times stronger than the scaling relation predicts. Recent 3D-MHD flare calculations explain this with a steeper slope $m \simeq 3$ for powerful flares, but this requires magnetic field strength inside active regions of $B_{\text{spot}} \simeq 10\text{--}20$ kG (J. Zhuleku et al. 2021). These MHD calculations predict surface-averaged magnetic field $\langle B \rangle$ values much higher than those observed thus far in nonsuperflaring PMS stars (K. R. Sokal et al. 2020).

To search for unusually strong surface magnetic fields in PMS superflaring stars—greater than any observed on a solar or stellar surface—we conducted a Chandra observation campaign in 2023 December. Within 1–3 days after the X-ray observations, we swiftly identified four super- and megaflaring young stars in the Orion Nebula region, which exhibited properties suitable for NIR Zeeman broadening measurements of magnetic-sensitive spectral lines, using data from the HET-HPF spectrograph. The SIMBAD names of these stars are COUP 881, COUP 1333, COUP 1424, and COUP 1463. The HPF spectra of these stars were obtained within a few weeks following the Chandra observations.

In this paper, among other findings, we present the stellar and X-ray flare properties of these four stars. Detailed measurements of their surface magnetic fields utilizing HPF data will be provided in a companion paper.

Investigating the effects of X-ray flares on disks' chemistry. Powerful PMS emission has a substantial impact on young stellar environments, influencing protoplanetary disk and planet formation processes. X-rays, along with ultraviolet (UV) radiation, ionize, heat, and photoevaporate protoplanetary disks and primordial planetary atmospheres. A myriad of astrophysical processes may ensue in planet-forming disks: enhanced magnetorotational instability affecting gas turbulence, viscosity, accretion, and planetary migration; ion-molecular chemistry; dust grain sputtering; and disk corona ionization producing jets and winds. Most of these X-ray ionization effects are theoretical (A. E. Glassgold et al. 2000, 2007; R. Alexander et al. 2014; J. E. Owen 2019; B. Ercolano et al. 2021; P. Woitke et al. 2024), but ionization products like [Ne II] and variable HCO^+ have been observed in some disks (C. C. Espaillat et al. 2023; A. R. Waggoner et al. 2023). Moreover, CMEs and stellar energetic particles associated with powerful X-ray flares might further intensify the chemical changes in disks and planets, as well as lead to the removal of disks and planetary atmospheres (V. S. Airapetian et al. 2020; J. D. Alvarado-Gómez et al. 2022; G. Hazra et al. 2022; V. Airapetian et al. 2023).

Most theoretical studies assume steady X-ray irradiation of disks without considering the high-amplitude variations in flux and spectrum due to large X-ray flares (U. Gorti & D. Hollenbach 2009; J. E. Owen 2019). Recent time-dependent calculations show that disk ionization may respond to sudden X-ray flares (C. Rab et al. 2017; A. R. Waggoner & L. I. Cleves 2022; V. Brunn et al. 2024; H. Washinoue et al. 2024). HCO^+ is one of

the most abundant molecular ions in protoplanetary disks, and its optically thin isotopologue H^{13}CO^+ is generally bright. Rapid (on timescales of weeks) HCO^+ abundance changes are theoretically predicted and can be explained by X-ray flares ionizing H_2 gas, producing H_3^+ , which reacts with CO to produce HCO^+ . Variable H^{13}CO^+ emission has indeed been detected by ALMA in the disk around the young star IM Lup, but no X-ray observations have been performed in the same epoch as the H^{13}CO^+ variability (L. I. Cleeves et al. 2017).

To investigate rapid changes in HCO^+ abundance due to the impact of large X-ray flares, we identified four young X-ray flaring stars in the Orion region (COUP 414, COUP 561, COUP 1174, and COUP 1333) during our 2023 December observation campaign, which have previously been measured for continuum dust and/or gas emission. We followed up on these stars with multiple ALMA observations over the following weeks.

In this paper, among other findings, we present the stellar and X-ray flare properties of these four stars. Detailed ALMA-based measurements of the temporal evolution of H^{13}CO^+ and/or HC^{18}O^+ in their disks will be provided in a companion paper.

Hunting for CMEs associated with large X-ray flares. The impact of megaflares—X-rays and extreme-UV (EUV) CME shocks and associated energetic particles—on photoevaporation, erosion, and chemistry of primordial planetary atmospheres is being studied via theoretical models, but with a few empirical constraints (e.g., V. S. Airapetian et al. 2020). It seems likely that steady (nonflare) stellar X-ray and ultraviolet (XUV) radiation destroys primordial atmospheres of inner planets much faster ($<10^7$ yr) than hydrogen thermal hydrodynamic escape (10^8 yr), but the role of megaflares is largely unknown. We might expect that PMS megaflares produce unusually powerful CMEs that might ionize, heat, entrain, and ablate young planetary atmospheres, leading to even more rapid mass loss.

The signatures of CMEs have been indirectly inferred in over 20 active G, K, and M dwarf stars through the presence of Doppler shifts in emission and absorption lines (C. Argiroffi et al. 2019; K. Namekata et al. 2021, 2024), as well as possible X-ray dimming and changes in X-ray absorption during flares (S.-P. Moschou et al. 2019; A. M. Veronig et al. 2021). The latter effect has not been seen in super- and megaflares produced by Orion Nebula PMS stars (F. Favata et al. 2005; K. V. Getman et al. 2008a).

Direct detection of CMEs from PMS megaflares may be possible in the radio band. At early phases of CME development, nonthermal Type II, III, and IV solar radio bursts are often seen at kilohertz to megahertz frequencies (E. P. Carley et al. 2020), and at late phases, when the CME occupies a large volume, thermal bremsstrahlung at higher frequencies of megahertz–gigahertz is expected. While numerous radio bursts in active M dwarfs have been detected, none could be clearly associated with CME shock plasma emission (J. Villadsen & G. Hallinan 2019). But the Orion Nebula PMS megaflares are orders of magnitude more powerful than these dMe flares.

CME emission associated with Orion Nebula megaflares could be detected as a rise and fall of radio flux, possibly with frequency drift, over days following the X-ray megaflares. This emission would be spatially resolved and displaced from the star on scales ≥ 1 au. During our 2023 December campaign, two VLBA observations were conducted in the 4 and 7 GHz bands within 1 to several days after the Chandra observations,

capturing radio emission from several dozen X-ray super- and megaflaring Orion Nebula stars.

The stellar and X-ray flare properties of these stars are reported in the current paper. Detailed VLBA-based astrometric analysis of CME-related emission due to potential wobbles in the radio positions of the flaring stars will be presented in a companion paper.

Examining the multi-epoch behaviors of both characteristic and flare X-ray emission. Long-term (on timescales ranging from a few to several tens of years) variations in PMS characteristic X-ray emission could be linked to magnetic cyclic activity.

Dynamo-generated magnetic fields undergo complex evolution within stellar interiors. In the current Sun, such processes follow an 11 yr cycle, causing observed variations in magnetic flux and associated sunspot numbers, the spatial distribution of sunspots, solar radiation, material ejection, and even the reversal of the Sun’s magnetic polarity. Recent 3D HD and MHD simulations successfully reproduce many observed features of solar-type magnetic cyclical activity (P. J. Käpylä et al. 2023). Many old cool stars with tachocline dynamos are known to exhibit cyclic activity. For instance, a study examining Ca II H and K lines has revealed variations in chromospheric activity among more than 100 F1-M2 main-sequence stars, resulting in cyclic periods spanning years to decades (S. L. Baliunas et al. 1995). XMM and Chandra X-ray studies have reported observed variations in X-ray activity, supporting cycles lasting from 1.6 to 19 yr in solar-type stars, including α Cen A and B, 61 Cyg A, HD 81809, ι Hor, and ϵ Eridani (J. Robrade et al. 2012; S. Orlando et al. 2017; J. Sanz-Forcada et al. 2019; M. Coffaro et al. 2020; T. Ayres 2023).

For fully convective old M dwarfs and young PMS stars, with their magnetic fields generated via convection-driven dynamos, simulations also predict magnetic cycles (R. K. Yadav et al. 2016; C. Emeriau-Viard & A. S. Brun 2017; B. P. Brown et al. 2020; P. J. Käpylä 2021). And, indeed, magnetic cyclic activity has been observed in a dozen fully convective old M dwarfs (B. J. Wargelin et al. 2017; R. V. Ibañez Bustos et al. 2019, 2020; Z. A. Irving et al. 2023).

To date, there are no reported observations of long-term cyclic activity in young PMS stars. In the current paper, the characteristic X-ray emission fluxes of a few hundred Orion PMS stars are identified and compared across four different epochs. A subsample of several diskless stars exhibiting the highest variations of their X-ray characteristic levels is selected for future periodogram analysis. This analysis will involve nearly 80 additional archived Chandra ACIS-HETG observations of the ONC, covering a time span of 20 yr.

In parallel, examining the multi-epoch behavior of large PMS X-ray flares can shed light on the crucial question of whether such flaring is ubiquitous or confined to a subset of stars. In the former scenario all protoplanetary disks and nascent planets around very young stars are subject to millions of violent high-energy irradiation events (K. V. Getman & E. D. Feigelson 2021), while in the latter case the significance of the impact of large flares on stellar environments will be much more limited. The current study addresses this question by providing evidence supporting the former scenario.

1.3. Outline of the Paper

Section 2 details the process of Chandra data reduction and point-source extraction. Section 3 introduces the sample of young stars analyzed in this study. Section 4 presents the identification of

Table 1
Chandra Observations

ObsID	Exposure (ks)	PI	Start Date (UT)
(1)	(2)	(3)	(4)
4395	99.95	Feigelson	2003-01-08 20:57:16
3744	164.16	Feigelson	2003-01-10 16:16:36
4373	171.47	Feigelson	2003-01-13 07:33:40
4374	168.98	Feigelson	2003-01-15 23:59:34
4396	164.55	Feigelson	2003-01-18 14:33:45
3498	69.05	Murray	2003-01-21 06:09:25
13637	27.24	Forbrich	2012-10-02 07:00:39
14334	8.37	Forbrich	2012-10-03 12:51:52
14335	25.93	Forbrich	2012-10-04 08:19:03
15546	17.83	Forbrich	2012-10-05 10:41:00
17735	88.9	Guenther	2016-11-27 02:11:50
26974	10.95	Getman	2023-12-17 04:26:31
29116	13.91	Getman	2023-12-17 19:50:05
29117	11.93	Getman	2023-12-18 04:53:32
27059	9.96	Getman	2023-12-20 23:26:34
29127	11.23	Getman	2023-12-21 06:10:36
29128	9.47	Getman	2023-12-22 10:51:25

Note. All observations were conducted in the VFAINT mode with the same aimpoint, located near the center of the ONC at $(\alpha, \delta) = (05:35:16.7, -05:23:24.0)$ J2000.0. Columns (1)–(4): the Chandra observation ID, net exposure time, name of the observation’s principal investigator, and start time of the observation in UT.

large X-ray flares and baseline segments, along with the computation of associated energetics. Section 5 focuses on various scientific analyses, including an investigation into the basic energy properties of large X-ray flares, a description of stars targeted by HET/ALMA/VLBA and their Chandra X-ray flares, a search for signs of magnetic cyclic activity, and an examination of multi-epoch behaviors of large X-ray flares. Section 6 summarizes our findings. The Appendix presents an evaluation of the temporal increase in the apparent Chandra X-ray median energies (MEs) of young Orion Nebula stars due to Chandra’s sensitivity degradation.

2. X-Ray Observations and Data Extraction

The X-ray data analyzed and discussed in this paper were acquired utilizing the Chandra X-ray Observatory (M. C. Weiskopf et al. 2002). The investigation involves 17 Chandra observations detailed in Table 1, obtained with the imaging array of the Advanced CCD Imaging Spectrometer (ACIS-I). This array consists of four abutted 1024×1024 pixel² front-side-illuminated charge-coupled devices, covering approximately $17' \times 17'$ on the sky (G. P. Garmire et al. 2003). The observations were conducted during various epochs: six during 2003 January as part of the COUP project, four in 2012 October, one in 2016 November, and six in 2023 December. Notably, the net Chandra exposure of the COUP project in 2003, totaling 838 ks, is about 10 times longer than the net exposures of each of the three subsequent programs, which range between 67 and 89 ks.

For the Chandra data reduction and analysis, CIAO v4.15.2 (A. Fruscione et al. 2006), CALDB v4.10.7, and HEASOFT v6.31.1 (Nasa High Energy Astrophysics Science Archive Research Center (Heasarc) 2014) were utilized.

During our 2023 December observation campaign, several data reduction tasks were employed to swiftly (within 1–2 days after a Chandra observation) analyze the new epoch-2023 Chandra data

and identify stars with large X-ray flares, facilitating the designation of targets for immediate follow-up observations with HET, ALMA, and VLBA. For this purpose, basic Chandra data processing steps were conducted, including reprocessing from L_1 to L_2 event data, generating exposure maps, conducting a rapid search for bright point sources using the wavelet transform method (P. Freeman et al. 2001), correcting astrometry based on the COUP source catalog, and extracting data for several hundred sources using CIAO’s `srcflux` tool. The source extraction process was simple, utilizing circular apertures for the sources while employing a single common background region. Subsequently, the resulting X-ray light curves were compared with the COUP source atlas (Figure Set 12; K. V. Getman et al. 2005b) to identify some young stars exhibiting prominent flares.

Later, we conducted a more thorough and consistent reduction and analysis of data from all 17 Chandra observations listed in Table 1. Our approach to X-ray data reduction follows established procedures outlined in various previous Chandra studies of dense stellar clusters (e.g., M. A. Kuhn et al. 2013; L. K. Townsley et al. 2014; K. V. Getman et al. 2017; L. K. Townsley et al. 2019; K. V. Getman et al. 2022).

Compared to the analysis conducted in 2023 December, we employed more sophisticated yet time-intensive methods for source identification and extraction. Specifically, we utilized maximum likelihood image deconvolution with local point-spread functions (PSFs) to enhance the resolution of closely spaced sources (P. S. Broos et al. 2010). Additionally, we employed the ACIS Extract (AE) software package, version 5658 2022 January 25 (P. S. Broos et al. 2010; P. Broos et al. 2012), to extract and characterize point sources from multi-ObsID ACIS data, based on local PSFs.

Through multiple iterations involving spatially crowded source candidates, AE generated optimal source and background extraction regions, refined source positions, distinguished between spurious and significant sources, and provided Poisson calculations for various X-ray properties of the sources, including net counts, MEs, and apparent photometric fluxes, among other parameters.

The original COUP catalog, based on the 2003 January Chandra ACIS-I data, contains 1616 X-ray point sources, with 1414 identified as young stellar members of the Orion Nebula region (K. V. Getman et al. 2005a, 2005b). Our current *automatic* reanalysis of these data identifies 1557 X-ray point sources, including 1348 COUP young stellar members. For the epochs in 2012, 2016, and 2023, AE produced lists of 1147, 1074, and 1029 X-ray point sources and recovers 975, 941, and 842 known COUP young stellar members, respectively. The multi-epoch Chandra images of the Orion Nebula region reveal hundreds of bright X-ray PMS stars (Figure 1).

3. PMS Stellar Sample

For the analysis of PMS X-ray emission presented in this paper, the initial multi-epoch sample of over 800 young stars from the Orion Nebula was narrowed down to a subset comprising relatively bright stars, each having at least 100 X-ray net counts in the epoch-2023 Chandra observations. This refined subsample consists of 245 young stars. Table 2 provides an overview of their fundamental stellar characteristics, encompassing spectral types, source extinctions, stellar masses and radii, Spitzer-IRAC spectral energy distribution (SED) slopes, stellar rotation velocities, and COUP time-averaged X-ray MEs and X-ray luminosities. IRAC SED slopes serve as indicators of disk presence or absence. The

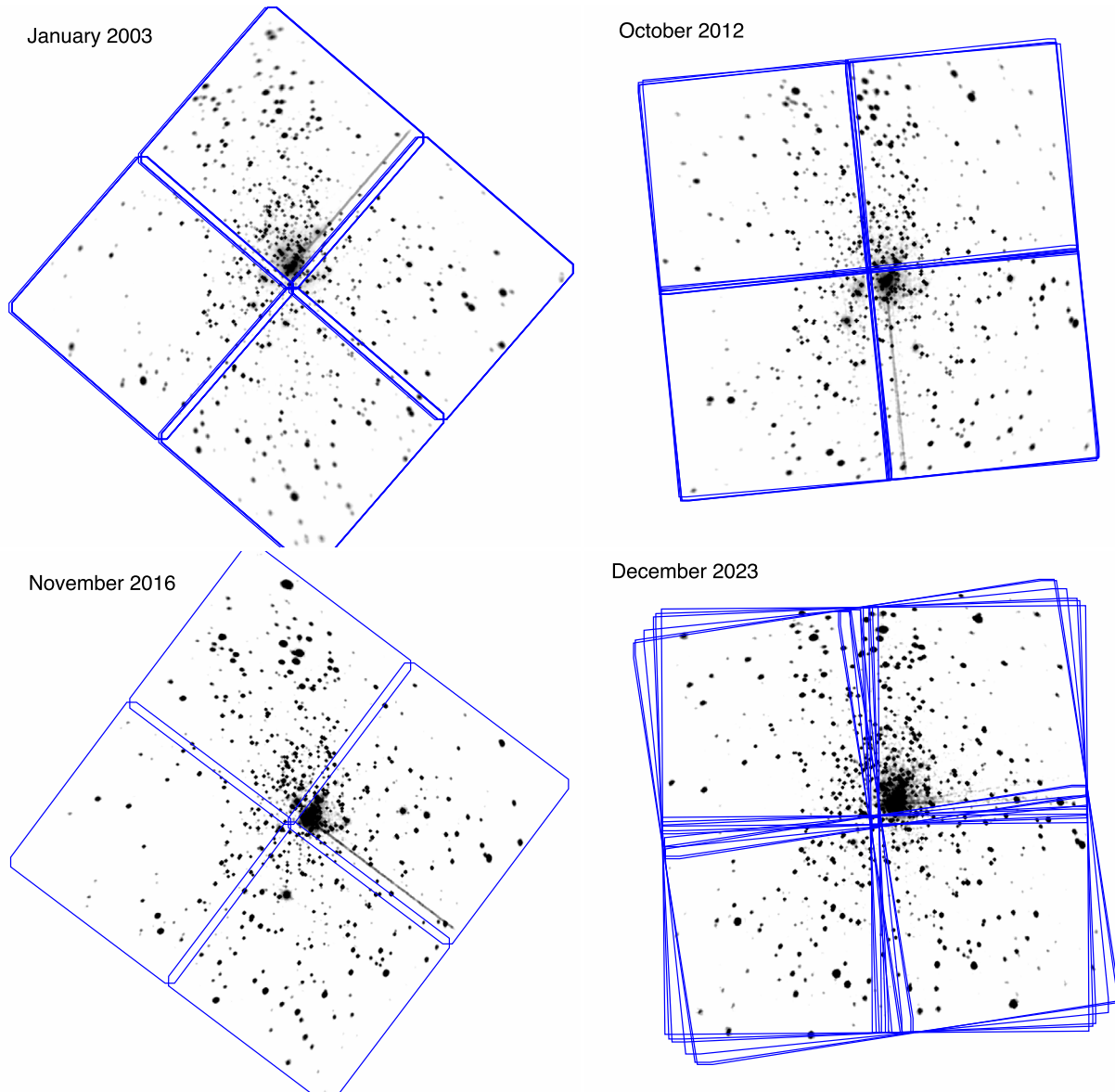


Figure 1. Low-resolution, smoothed Chandra ACIS-I images of the Orion Nebula region presented for each of the four distinct epochs of observations: 2003 January, 2012 October, 2016 November, and 2023 December. The images are given for the 0.5–8 keV energy band. Each panel represents the combined view of multiple observations conducted during the corresponding epoch, with $17' \times 17'$ fields of view for each observation outlined in blue. Due to variations in roll angles among observations within each epoch, the merged images sometimes display polygonal shapes rather than perfect squares.

X-ray ME serves as a proxy for both coronal plasma temperature and absorbing gas column density (K. V. Getman et al. 2010).

Among the 245 stars, estimates are available for 80% of their spectral types, 95% of their masses, 85% of their IRAC SED slopes, and 65% of their rotation quantities (either periods or projected rotation velocities). Regarding spectral types, 38% are classified as M-type stars, 48% as K-type stars, 9% as G-type stars, and 5% as A- to O-type stars. The stellar masses in the sample range between 0.1 and $40 M_{\odot}$, with a median value of $1.2 M_{\odot}$. Similarly, stellar radii span from 1 to $9 R_{\odot}$, with a median value of $2.5 R_{\odot}$. And time-averaged COUP X-ray luminosities span from $8.7 \times 10^{28} \text{ erg s}^{-1}$ to $1.6 \times 10^{33} \text{ erg s}^{-1}$, with a median value of $3.1 \times 10^{30} \text{ erg s}^{-1}$.

Among stars with known IRAC SED slopes, 58% are categorized as disk bearing, while 42% are identified as diskless. Disk-bearing stars typically exhibit systematically

slower rotation owing to star–disk magnetic coupling (S. P. Matt et al. 2015; C. Garraffo et al. 2018). Specifically, for diskless and disk-bearing stars, the median rotation velocities are 29 and 16 km s^{-1} , respectively, and the median rotation periods are 5 and 9 days, respectively.

4. X-Ray Light Curves and Identification of Flare and Characteristic Segments

Figures 2 and 3 showcase sample pages from two flare atlases, displaying X-ray photon arrival diagrams and light curves. The complete atlases for all 245 stars are accessible as electronic Figure Sets 2 and 3. The sample pages in Figures 2 and 3 specifically highlight the lightly absorbed, diskless star of type M1, COUP 43, a member of the ONC cluster. The star exhibited large X-ray flares during the epochs of 2003 and 2023.

Table 2
Stellar Properties of 245 Stars Selected as the X-Ray Brightest in the 2023 Epoch

Src.	R.A.	Decl.	SpT	A_V	M	R	α_{IRAC}	P_{rot}	$v_{\text{rot}} \sin(i)$	ME	$\log(L_X)$
(1)	(deg)	(deg)	(4)	(mag)	(M_{\odot})	(R_{\odot})	(8)	(days)	(km s^{-1})	(keV)	(erg s^{-1})
COUP23	83.688341	−5.417808	K2	3.3	2.4	3.4	−2.8	3.5	32.9	1.3	31.2
COUP28	83.693401	−5.408844	M0	0.0	0.7	1.7	−2.6	...	22.7	1.4	30.8
COUP43	83.703485	−5.388333	M1	2.1	0.9	2.2	−2.5	...	70.6	1.3	30.3
COUP66	83.716877	−5.411919	M3.5e	2.3	0.8	1.6	−1.1	...	13.8	1.4	30.2
COUP67	83.717473	−5.375534	M2.5	2.3	0.9	2.7	−1.8	...	11.6	1.2	30.3
COUP107	83.733255	−5.386967	K1e	−2.8	17.4	10.3	1.3	31.3
COUP108	83.733330	−5.490630	M1.5	2.4	1.1	1.8	−2.8	1.9	27.9	1.4	30.4
COUP112	83.735615	−5.464103	M2e	1.4	0.8	1.2	−1.4	6.5	15.4	1.3	30.4
COUP115	83.736866	−5.360111	K7	8.5	2.0	2.5	−2.6	3.4	19.0	1.7	30.6
COUP124	83.740827	−5.397962	K8	3.5	2.3	3.4	−1.6	...	19.2	1.4	30.9

Note. Only a few examples of the table entries are given here; the full machine-readable table for all 245 young stars is provided in the electronic edition of this paper. Columns (1)–(3): source name, R.A., and decl. for epoch J2000.0, from K. V. Getman et al. (2005b). Column (4): spectral type from B. A. Skiff (2014). Columns (5)–(7): source’s visual extinction, stellar mass, and radius are from Table 6 of K. V. Getman et al. (2022). These quantities were obtained utilizing NIR photometry data and the PARSEC 1.2S PMS stellar evolutionary model of A. Bressan et al. (2012) and Y. Chen et al. (2014). Column (8): SED slope based on the Spitzer-IRAC data from S. T. Megeath et al. (2012). Values of α_{IRAC} less than -1.9 and greater than or equal to -1.9 indicate diskless and disk-bearing stars, respectively. Columns (9)–(10): stellar rotation information. Stellar rotation periods are obtained from the compilation of C. L. Davies et al. (2014). Projected stellar rotation velocities, derived from APOGEE NIR spectral data, are sourced from M. Kounkel et al. (2019). Columns (11)–(12): X-ray ME and time-averaged X-ray luminosity are based on the COUP data of K. V. Getman et al. (2005b). For relatively faint X-ray stars, improved X-ray luminosities are from K. V. Getman et al. (2022).

(This table is available in its entirety in machine-readable form in the [online article](#).)

The raw (unbinned) event data from each of the 17 Chandra observations, delivered by AE, underwent processing using the R-based `bayesian_blocks.R` code.¹² This process yields an optimal segmentation of the data, identifying relevant time change-points. The code implements the Bayesian Blocks algorithm (J. D. Scargle 1998; J. D. Scargle et al. 2013), widely utilized in astronomy for flare identification (K. V. Getman & E. D. Feigelson 2021). The algorithm partitions the data into blocks of varying widths, striking a balance between the goodness-of-fit of the blocks and the complexity of the partitioning. Goodness-of-fit is determined using the Cash maximum likelihood statistic, which is suitable for sparse Poisson-driven data points (W. Cash 1979). The complexity of the partitioning is controlled by the prior distribution of the change-points in the form $\log(\text{Prior}) = 4 - \log(73.6 \times p0 \times N^{-0.5})$, where $p0$ is the scaling factor responsible for the algorithm’s sensitivity and N is the number of data points in the time series. In instances where the resulting number of blocks exceeded 10, we iteratively adjusted the slope of the prior distribution to provide a simpler solution.

The inferred Bayesian Blocks segments with their 1σ uncertainty ranges based on the N. Gehrels (1986) statistic are depicted in both flare atlases and are listed in Table 3. These segments were utilized for the identification of X-ray characteristic and large flare emission levels and calculation of the characteristic X-ray luminosity and energetics of large X-ray flares, as described below.

Additionally, the flare atlases include kernel density estimation (KDE) smooth curves shown in red.¹³ It is important to note that these curves are intended solely as visual aids to

illustrate potential trends in X-ray emission rise and decay. They do not, however, establish the statistical significance of related variability features.

For each source, the X-ray count rates corresponding to the Bayesian Blocks segments were translated into intrinsic X-ray luminosities in the 0.5–8 keV energy band (L_X). This conversion was achieved using AE-based instrument-independent and PSF-corrected apparent X-ray photon fluxes ($F_{X,\text{phot}}$), expressed in units of $\text{photons cm}^{-2} \text{s}^{-1}$, and a singular conversion factor derived from $F_{X,\text{phot}}$ to L_X . The conversion factor was based on the time-averaged X-ray luminosity values extracted from the COUP data set (Table 2). No adjustments were made for the effects of X-ray emission hardening during large X-ray flares. According to the calculations utilizing the Portable Interactive Multi-Mission Simulator (PIMMS¹⁴), the X-ray hardening effect resulting from the heightened coronal plasma temperature (e.g., from 2 to 10 keV) during a significant X-ray flare (K. V. Getman et al. 2008a) will yield only a 5% increase in the intrinsic X-ray luminosity for the same observed Chandra count rate.

Graphical output from Figure Sets 2 and 3 was examined, and the Bayesian Blocks segments with the lowest L_X values were chosen to represent the X-ray characteristic emission levels (see Column (9) in Table 3). The L_X values of these segments, averaged across each observation epoch and weighted by the segments’ durations, constitute the characteristic X-ray luminosities ($L_{X,\text{char}}$). These are detailed in Table 4 and depicted as horizontal dashed lines in Figure Set 3.

Segments with X-ray luminosities more than three times higher than the characteristic luminosities were categorized as either short impulsive flares or large powerful flares. In Figure Set 3, these segments are highlighted in red. Subtracting the characteristic levels and integrating the X-ray luminosities of such segments over their durations yields flare energies, denoted as $E_{X,\text{fl}}$ (see Table 4). For the observation epochs of

¹² The code is available at <https://github.com/AlicePagano/ASPA-Project-Bayesian-Blocks-Algorithm-in-R>.

¹³ These are constructed using R’s function `density(x, kernel = "epanechnikov", cut = 0)`. The Epanechnikov kernel is optimal in a least-squares sense (M. P. Wand & M. C. Jones 1994). It is well established that the KDE method underperforms near data boundaries (M. L. Hazelton & J. C. Marshall 2009). To address this, we apply the data reflection technique, where data points are reflected at the boundaries, effectively extending the data set beyond its original range. This approach helps mitigate boundary effects by providing additional density support near the edges.

¹⁴ The tool is available online at <https://heasarc.gsfc.nasa.gov/cgi-bin/Tools/w3pimms/w3pimms.pl>.

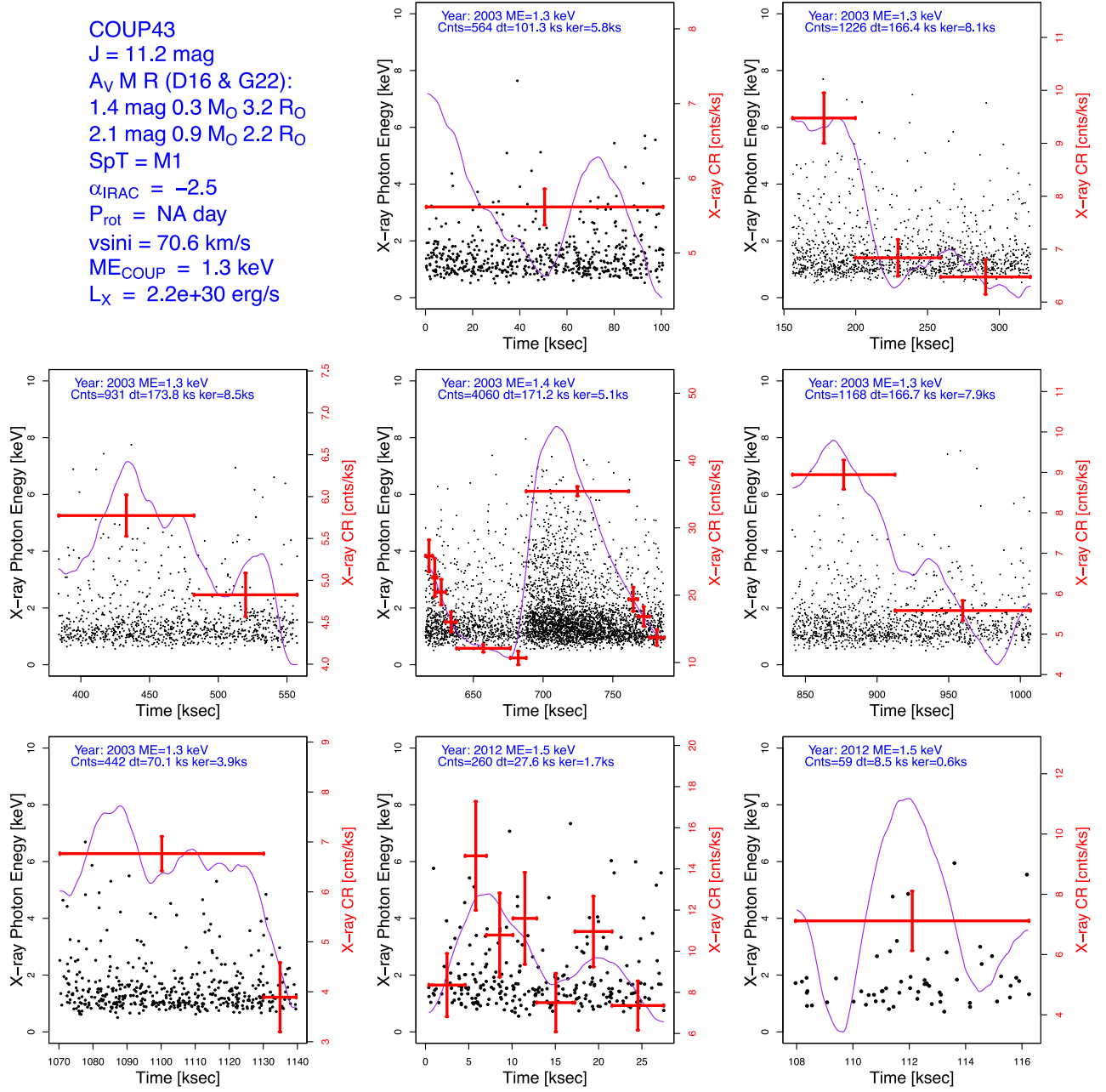


Figure 2. Sample page from the flare atlas of Figure Set 2 featuring COUP 43. This atlas includes basic stellar properties extracted from Table 2, along with additional extinction–mass–radius estimates from N. Da Rio et al. (2016). It also showcases X-ray photon arrival diagrams and apparent light curves in count rates for each of the 17 Chandra observations listed in Table 1. The abscissa time values are in kiloseconds, and each of the four-epoch observation sets begins at time 0 ks. Black points on the photon arrival diagrams represent individual X-ray photons, with their energy values in keV shown on the left ordinates. Red segments and magenta curves denote parts of the light curves, with units of counts per kilosecond displayed on the right ordinates. The red segments are outcomes from the Bayesian Blocks analysis, discussed further in the text. The magenta KDE curves, also discussed in the text, provide visual insights into the light-curve trends. The figure legends include observation epochs, total number of X-ray photons per observation, ME of the photons, observation duration, and width of the KDE kernel. 1σ error bars for the Bayesian Blocks are based on the N. Gehrels (1986) statistic. The time zero-points on the graphs for the epochs of 2003, 2012, 2016, and 2023 correspond to MJD values of 52647.89, 56202.31, 57719.11, and 60295.20 days, respectively. Refer to the next page for the continuation of the figure.

(The complete figure set (245 images) is available in the [online article](#).)

2012 and 2023, the $E_{X,fl}$ values associated with large X-ray flares represent only lower limits of the true energy values, given that the durations of individual 2012 and 2023 Chandra observations are shorter than the typical durations of large PMS X-ray flares, which range from 40 to 50 ks (K. V. Getman et al. 2008a, 2021).

In the observations of 2003, 2012, 2016, and 2023, there are 222, 100, 44, and 157 identified X-ray flare events among

the 245 young stars (Table 4), respectively, with energies exceeding $\log(E_{X,fl}) > 34$ erg. The relatively low number of flares with inferred energy values recorded in 2016 can be attributed to the shorter total time span (including observation gaps), resulting in fewer reliable characteristic segments and thus making it difficult to accurately determine flare energies.

Lastly, segments with X-ray luminosities falling between the levels of flares and characteristic emission were categorized as

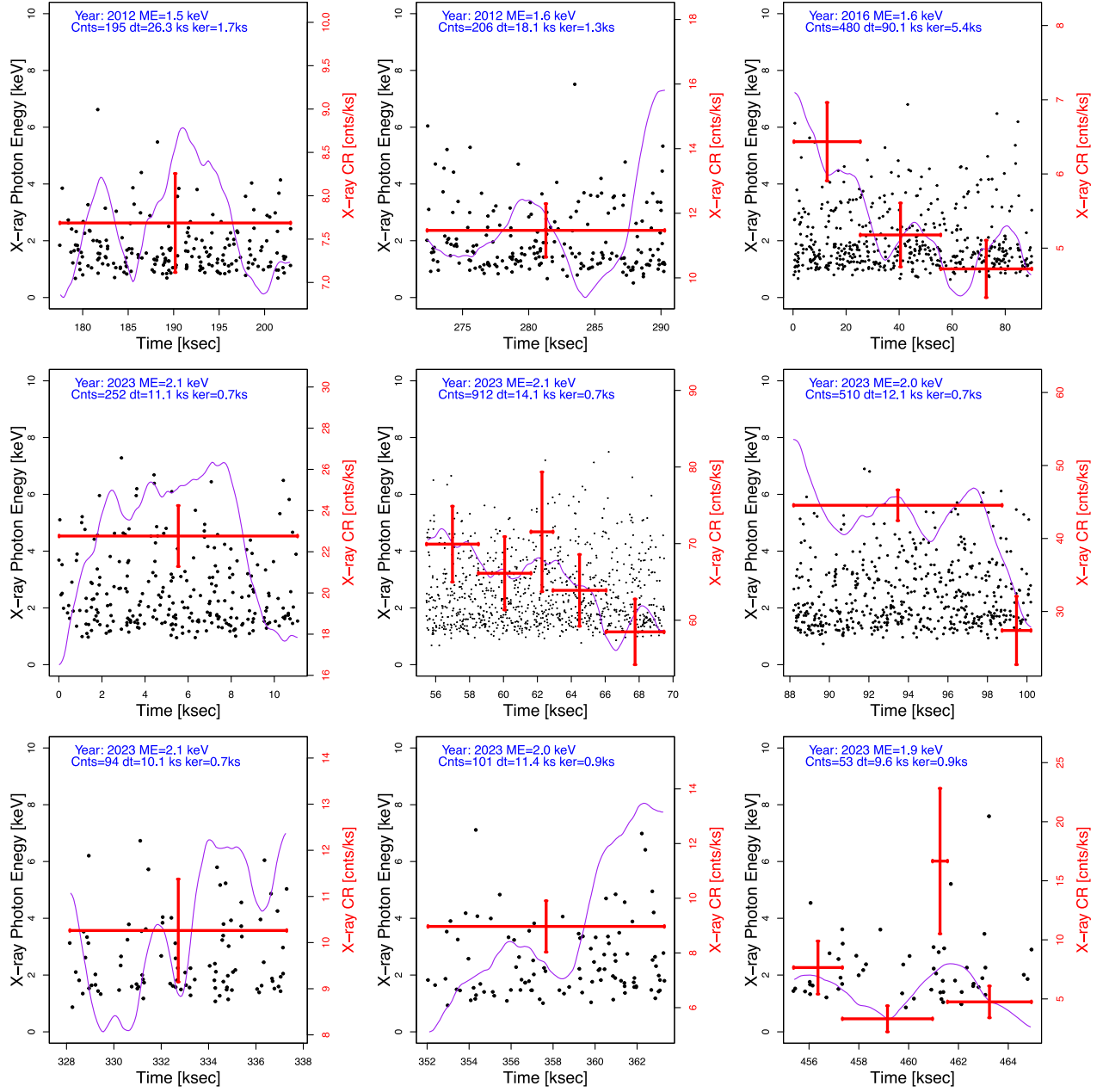


Figure 2. (Continued.)

“mildly variable.” The combined energy from these segments, along with the flare segments, is denoted as $E_{X,var}$ and detailed in Table 4.

In Figure Set 2, the stellar property legends include additional estimations for source extinction, stellar mass, and stellar radius from N. Da Rio et al. (2016), which are based on NIR data obtained with the APOGEE spectrograph and older PMS evolutionary models by L. Siess et al. (2000). When compared to the stellar properties from K. V. Getman & E. D. Feigelson (2021), as listed in Table 2 and derived based on NIR photometry and newer PARSEC PMS evolutionary models, the masses and radii from Da Rio appear systematically lower and higher, respectively, by approximately 30% and 15%. This systematic difference primarily stems from variations in the utilized PMS models and the adoption of different color- T_{eff} relations, as detailed in Appendix C of

K. V. Getman & E. D. Feigelson (2021). We adopt the stellar properties from K. V. Getman & E. D. Feigelson (2021) here simply because they are available for a larger number of stars.

Mainly due to the buildup of contamination on the optical blocking filters, the sensitivity of Chandra ACIS toward softer X-rays has degraded over time. As a result, the apparent Chandra X-ray MEs of sources have increased over time. The values of the apparent ME provided in the panel legends of Figure 2 are especially useful for comparing these quantities among multiple Chandra observations taken during the same epoch. For instance, the ME of COUP 43 reached a peak value of 1.4 keV during a large X-ray flare (observation #4 for epoch 2003), while it remained constant at 1.3 keV during the other five Chandra observations, which primarily showed a characteristic level of X-ray emission in epoch 2003.

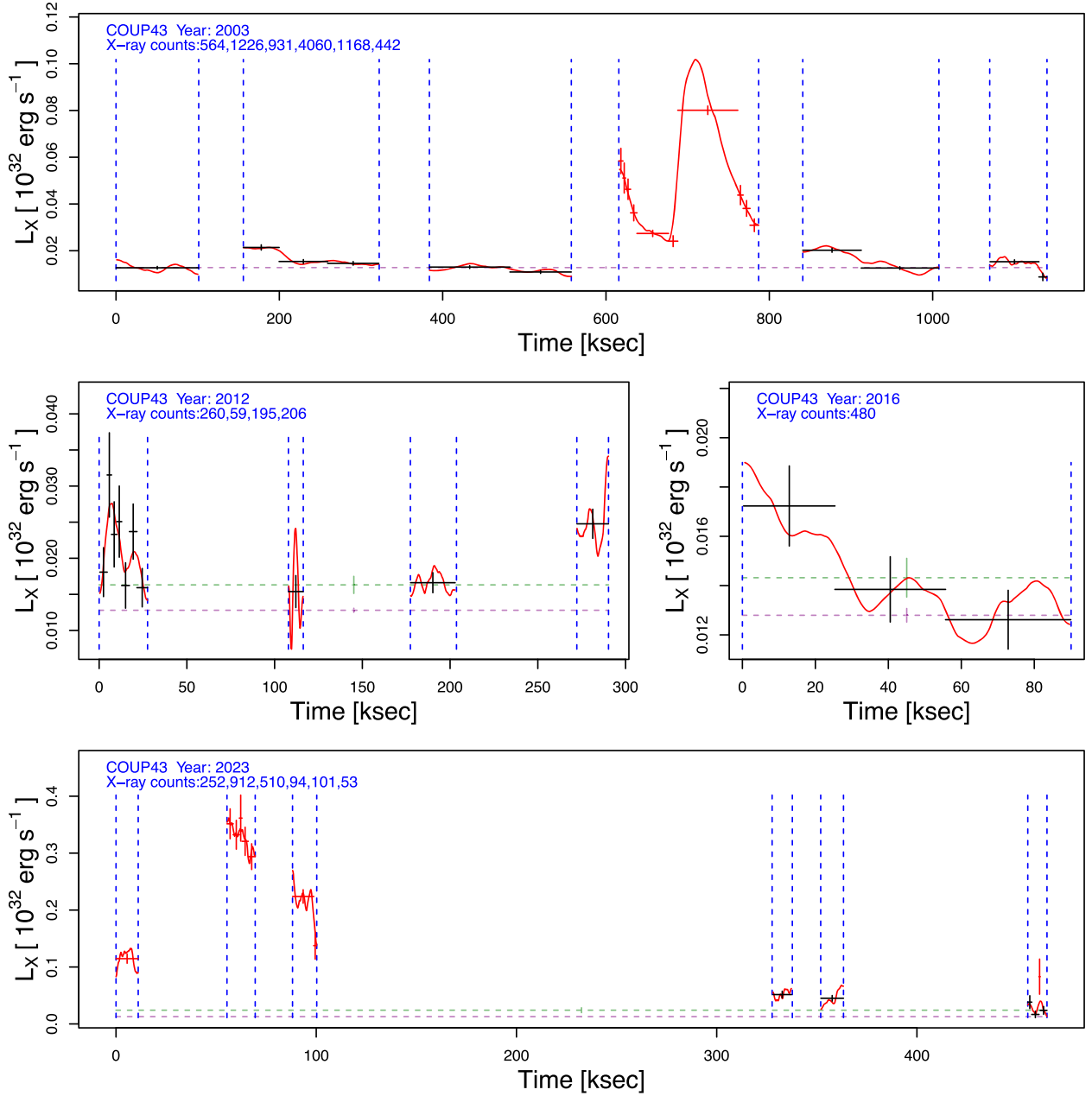


Figure 3. Sample page from the flare atlas of Figure Set 3 featuring COUP 43. The atlas showcases X-ray light curves in units of intrinsic stellar X-ray luminosity, presented as four separate figure panels, each corresponding to one of the four-epoch observation sets. The blue dashed lines indicate the start and stop times for each of the 17 Chandra observations listed in Table 1. The KDE curves are shown in red. The red and black Bayesian Blocks segments represent cases of strong or mild to no variability, respectively. The former denote short X-ray impulsive or long powerful flares, while the latter indicate characteristic emission or mild flare levels. The characteristic emission levels are also marked by dashed lines: magenta for the epoch 2003 and green for the 2012, 2016, and 2023 epochs. Standard 1σ confidence intervals (marked by error bars) for the Bayesian Blocks and characteristic levels are based on the N. Gehrels (1986) statistic. The figure legends include observation epochs and total number of X-ray photons per observation. (The complete figure set (245 images) is available in the [online article](#).)

However, for interepoch comparisons of a source’s ME, it is important to account for systematic shifts, which we derive in the [Appendix](#).

5. Results

5.1. Basic Energy Properties of Detected Large X-Ray Flares

Figures 4(a)–(d) depict the energy distributions of the large X-ray flares identified in this study (Table 4). They also illustrate the positive correlations between these flare energies and stellar mass and size, respectively, and no correlations

between flare energies and the presence or absence of protoplanetary disks.

These observed patterns in the distribution of flare energies align with findings from previous studies of large PMS X-ray flares, as discussed below.

Notably, Figure 4(a) illustrates that the energy distributions of flares observed during *late* epochs (2012, 2016, and 2023) exhibit consistency among themselves but are systematically shifted toward lower energies compared to those observed during the *early* epoch (2003). This discrepancy can be attributed to the decreasing frequency of stellar flares with

Table 3
Bayesian Blocks

Src.	Year	Obs. No.	t_{start} (ks)	t_{stop} (ks)	Counts	$\log(L_{X,\text{BB}})$ (erg s ⁻¹)	$\sigma_{\log(L_{X,\text{BB}})}$ (erg s ⁻¹)	Flag
(1)	(2)	(3)	(4)	(5)	(6)	(7)	(8)	(9)
COUP28	2003	1	0.08	101.20	592	30.09	0.018	c
COUP28	2003	2	156.07	322.27	865	30.04	0.015	c
COUP28	2003	3	383.91	431.60	282	30.10	0.027	n
COUP28	2003	3	431.60	435.83	99	30.70	0.046	f
COUP28	2003	3	435.83	527.55	760	30.24	0.016	n
COUP28	2003	3	527.55	531.65	90	30.67	0.048	f
COUP28	2003	3	531.65	534.17	88	30.87	0.049	f
COUP28	2003	3	534.17	557.53	2773	31.40	0.009	f
COUP28	2003	4	615.71	625.68	3834	31.91	0.008	f
COUP28	2003	4	625.68	636.53	3512	31.84	0.008	f
COUP28	2003	4	636.53	651.55	2806	31.60	0.009	f
COUP28	2003	4	651.55	677.62	2550	31.32	0.009	f
COUP28	2003	4	677.62	714.48	2453	31.15	0.009	f
COUP28	2003	4	714.48	716.02	62	30.93	0.059	f
COUP28	2003	4	716.02	717.24	61	31.03	0.059	f
COUP28	2003	4	717.24	786.90	2355	30.85	0.009	f
COUP28	2003	5	841.07	841.57	20	30.93	0.108	f
COUP28	2003	5	841.57	913.58	1777	30.72	0.011	f
COUP28	2003	5	913.58	913.89	18	31.09	0.115	f
COUP28	2003	5	913.89	1007.63	1850	30.62	0.010	f
COUP28	2003	6	1069.89	1111.01	525	30.43	0.020	n
COUP28	2003	6	1111.01	1139.98	293	30.33	0.026	n
COUP28	2012	1	0.05	27.53	126	29.96	0.046	c
COUP28	2012	2	107.85	116.29	36	29.93	0.082	c
COUP28	2012	3	177.43	203.20	147	30.06	0.043	n
COUP28	2012	4	272.38	290.26	81	29.96	0.056	c

Note. Examples of the table entries are provided for the 2003 and 2012 Chandra observations of COUP 28. The full machine-readable table, containing 8691 entries for all four epochs of observations of all 245 young stars, is available in the electronic edition of this paper. Columns (1)–(3): source name, epoch year, and the relative sequential numbering of Chandra observations within that epoch. Columns (4)–(9): properties of the identified Bayesian Blocks segment, including start and stop times of the segment, X-ray counts, X-ray luminosity level and its uncertainty, and a flag indicating the segment’s status: “f” for flare level, “c” for characteristic level, and “n” for mild variability between the flare and characteristic levels.

(This table is available in its entirety in machine-readable form in the [online article](#).)

Table 4
Flare Energetics

Src.	Year	$\log(L_{X,\text{char}})$ (erg s ⁻¹)	$\sigma_{\log(L_{X,\text{char}})}$ (erg s ⁻¹)	$\log(E_{X,\text{n}})$ (erg)	$\sigma_{\log(E_{X,\text{n}})}$ (erg)	$\log(E_{X,\text{var}})$ (erg)	$\sigma_{\log(E_{X,\text{var}})}$ (erg)
(1)	(2)	(3)	(4)	(5)	(6)	(7)	(8)
COUP23	2003	31.09	0.012	36.47	0.015
COUP23	2012	30.89	0.016	35.34	0.027
COUP23	2016	30.90	0.010
COUP23	2023	30.90	0.025	35.13	0.066
COUP28	2003	30.06	0.012	36.67	0.003	36.69	0.003
COUP28	2012	29.96	0.033	33.80	0.238
COUP28	2016	29.97	0.052	34.57	0.114
COUP28	2023	29.78	0.065	34.28	0.088	34.35	0.086
COUP43	2003	30.11	0.009	35.84	0.010	35.91	0.010
COUP43	2012	30.21	0.031	34.43	0.093
COUP43	2016	30.16	0.024
COUP43	2023	30.38	0.076	35.88	0.014	35.91	0.014

Note. Examples of the table entries are provided for a few stars. The full machine-readable table, containing 980 entries for all four epochs of observations of all 245 young stars, is available in the electronic edition of this paper. Columns (1)–(2): source name and epoch year. Columns (3)–(4): X-ray characteristic (baseline) level and its 1σ uncertainty. Columns (5)–(6): X-ray energy (and its 1σ uncertainty) of all large and/or impulsive flares (i.e., including only Bayesian Blocks marked in red in Figure 3). Columns (7)–(8): the total X-ray energy (and its 1σ uncertainty) for the sum of large flares and mild variable events, i.e., all Bayesian Blocks segments that are above the characteristic level. These include all Bayesian Blocks marked in red in Figure 3, as well as some Bayesian Blocks marked in black, which are identified as “mild variable.”

(This table is available in its entirety in machine-readable form in the [online article](#).)

increasing energy (K. V. Getman & E. D. Feigelson 2021). Consequently, the approximately 10-fold longer observations during the early epoch capture a higher number of relatively rare, more powerful flares. Note that our simple flare identification algorithm (see Section 4) treats all flares detected within a single epoch as a single flare event. Thus, the presence of extremely long and powerful flares predominates the observed flare energy distribution for the early epoch observations. Therefore, there appears to be an apparent lack of lower flare energies in the energy distribution curve for the early epoch, although this absence is not intrinsic.

Figure 4(a) further illustrates that the upper range of flare energy distribution during the early epoch can be adequately modeled by a Pareto function (B. Arnold et al. 1983), with the Pareto slope β approximately ranging between 0.9 and 1.

For a detailed examination of the properties of the Pareto function, refer to K. V. Getman & E. D. Feigelson (2021). Following K. V. Getman & E. D. Feigelson (2021), we conducted multiple trials using the early epoch flare energy data with various cutoff X-ray flare energies ($E_{X,\text{cutoff}}$). We applied the maximum likelihood estimation of the Pareto slope (formula (2) in K. V. Getman & E. D. Feigelson 2021), generated the Pareto distribution cumulative distribution function (CDF) using the estimated slope, and performed the Anderson–Darling (AD) test to compare the unbinned and truncated observed data ($>E_{X,\text{cutoff}}$) with the Pareto CDF. The AD p -values were then evaluated to determine whether $E_{X,\text{cutoff}}$ corresponds to the flare energy completeness limit. We found that AD p -values were all <0.01 for $E_{X,\text{cutoff}} < 10^{35.7}$ erg, indicating that the underlying Pareto distributions do not adequately represent the data. Conversely, for $E_{X,\text{cutoff}} \geq 10^{35.7}$ erg, AD p -values were above 0.1, suggesting that any of these cases can be used as reasonable solutions for the Pareto slopes. Statistical uncertainties on the Pareto slopes were estimated via bootstrap resampling. For example, with $\log(E_{X,\text{cutoff}}) = [35.7, 35.8, 35.9, 36.0]$ erg, the truncated data sets contain $N = [137, 117, 101, 80]$ flare energy points, yielding AD p -values of $[0.14, 0.22, 0.3, 0.22]$ and Pareto slopes of $\beta = [0.88 \pm 0.09, 0.93 \pm 0.09, 0.98 \pm 0.12, 1.00 \pm 0.13]$, respectively. Figure 4(a) illustrates the case of $\log(E_{X,\text{cutoff}}) = 35.8$ erg.

In the context of the energy distribution form ($dN/dE_X \sim E_X^{-\alpha}$), where $\alpha = \beta + 1$, this implies an α slope in the range of roughly 1.9–2.0. Remarkably, this slope value aligns with the flare energy distribution observed in various types of normal stars, including PMS stars, older stars, and even the Sun (M. Caramazza et al. 2007; J. F. Colombo et al. 2007; B. Stelzer et al. 2007; K. V. Getman & E. D. Feigelson 2021). The consistency in slope indicates a common flare production mechanism across all these stars.

Figures 4(b) and (c) demonstrate statistically strong positive correlations (with p -values from Kendall’s τ test of <0.0001) between flare energy and stellar mass/size for both early and late epochs. These and similar correlations, previously illustrated in Figure 6 of K. V. Getman et al. (2021), can be attributed to the nature of magnetic fields in fully convective PMS stars. Unlike solar-type main-sequence stars, where magnetic fields are generated in a thin tachocline layer (known as the $\alpha\Omega$ dynamo), fully convective PMS stars possess a distributed α^2 dynamo throughout their interior (M. K. Browning 2008; U. R. Christensen et al. 2009; P. J. Käpylä et al. 2023). In these fast-rotating stars, the strength of the surface magnetic field is determined by the kinetic energy of convective flows within the entire stellar interior, rather

than rotation (U. R. Christensen et al. 2009; A. Reiners et al. 2009; A. Reiners & U. R. Christensen 2010; A. Reiners et al. 2022). Consequently, larger PMS stellar volumes (and hence mass and surface area) result in stronger magnetic fluxes, larger coronal active regions, and three-dimensional extensions of X-ray-emitting structures (K. V. Getman et al. 2022, 2023). This explains not only the correlations between flare energy ($E_{X,\text{fl}}$) and mass for large flares but also the positive correlations between time-averaged stellar X-ray luminosities and mass (E. D. Feigelson et al. 1993; T. Preibisch et al. 2005; A. Telleschi et al. 2007; K. V. Getman et al. 2022). Remarkably, our current results on flare energetics show, complementing previous findings of K. V. Getman et al. (2021), that even smaller X-ray flares ($\log(E_{X,\text{fl}}) < 35$ erg) positively correlate with stellar mass/size, marking as the first for this type of observation.

Figure 4(d) demonstrates that the energetics of X-ray flares show no correlation with the presence or absence of disks. This observation aligns with previous findings by K. V. Getman et al. (2008b, 2021), who argued that the properties of large X-ray flares in PMS stars remain consistent regardless of the presence or absence of protoplanetary disks, as inferred from infrared photometry. This supports the solar-type model of flaring coronal magnetic loops, wherein both footpoints are anchored in the stellar surface rather than having one footpoint at the inner rim of the disk. Notably, our current flare energetics results extend this finding to less powerful X-ray flares ($\log(E_{X,\text{fl}}) < 35$ erg), marking the first time such disk independence has been demonstrated.

No correlation was found between PMS X-ray flare energies and stellar rotation rates (graph not shown). This lack of correlation aligns with expectations that the kinetic energy of convective flows and the generation of strong magnetic fields in fast-rotating PMS stars exhibit little to no dependence on rotation (U. R. Christensen et al. 2009; A. Reiners et al. 2022). Consistent with these findings, the time-averaged X-ray luminosities of fully convective PMS stars are also observed to be independent of rotation rates (T. Preibisch et al. 2005; F. Alexander & T. Preibisch 2012).

5.2. Stars and Their X-Ray Flares for HET, ALMA, and VLBA Studies

In this section, we outline the X-ray flaring stars, as well as the properties of their flares, identified in the 2023 December Chandra observations and subsequently observed with HET-HPF, ALMA, and VLBA.

Due to the nature of the 2023 December Chandra data, consisting of six short observations separated by significant gaps (see Table 1, Figure 3), there is generally a lack of rich X-ray photon statistics necessary for detailed time-resolved flare analysis and modeling (e.g., K. V. Getman et al. 2011, 2021). Additionally, information regarding the morphology and duration of the identified large X-ray flares is limited. To derive rough estimates of intrinsic X-ray flare properties, such as flare peak coronal plasma temperature (kT) and scale of flaring coronal loop (L), we reasonably assume that the 2023 December X-ray flares follow the trends observed in large COUP X-ray flares from the 2003 Chandra observations, as analyzed and modeled by K. V. Getman et al. (2008a, 2008b). Figures 4(e) and (f) display these trends. The trends are modeled using B-spline quantile regression, which offers enhanced flexibility for capturing nonlinear relationships (X. He & P. Ng 1999; P. T. Ng & M. Maechler 2007).

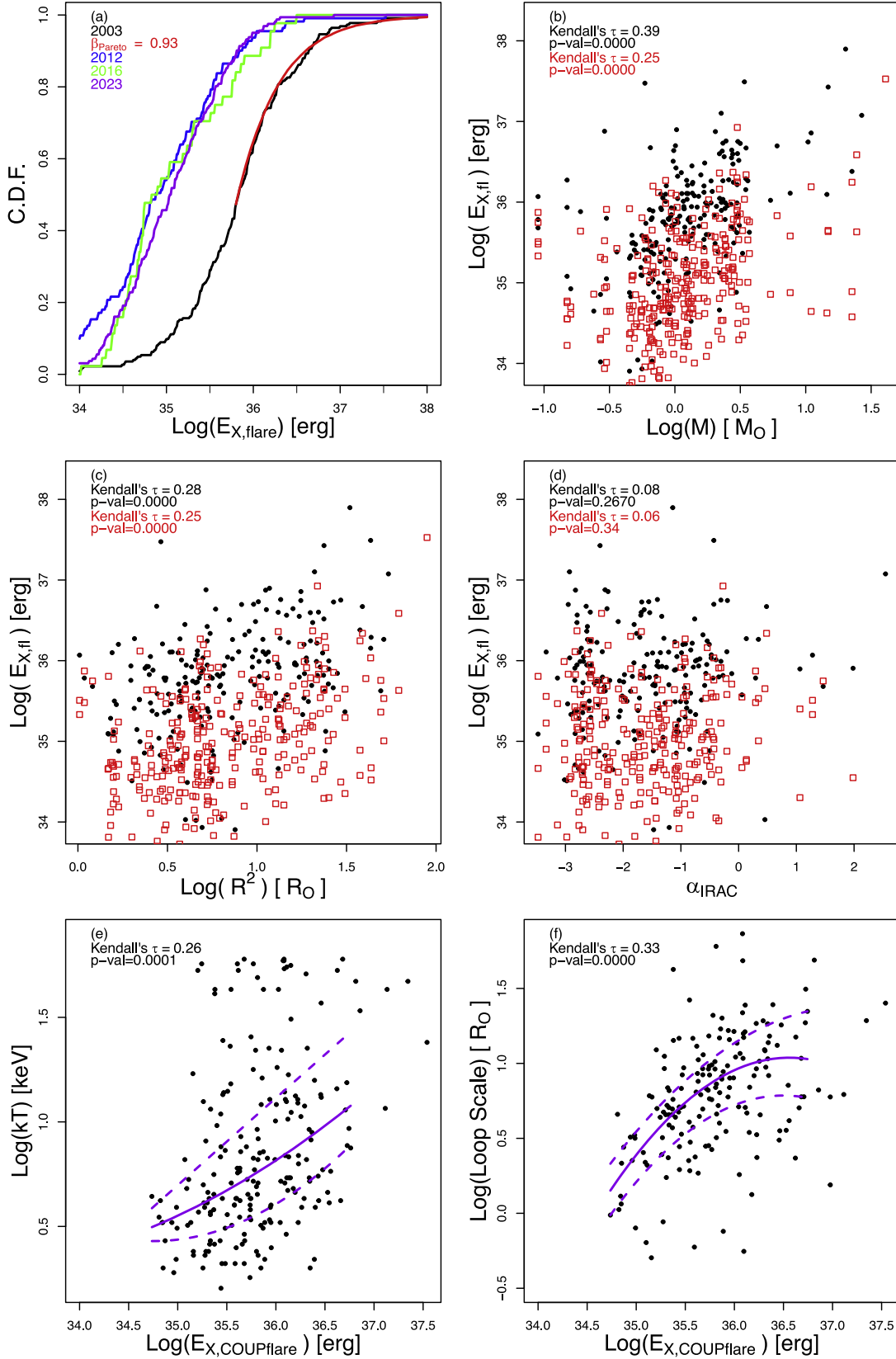


Figure 4. (a) CDFs illustrating the X-ray flare energy distributions for the 2003 epoch (in black) and later (2012, 2016, and 2023) epochs (in color). The bright end of the 2003 epoch CDF is fitted with the Pareto (power-law) function (red), with a slope of $\beta = 0.91$. (b)–(d) Scatter plots depicting the energies of X-ray flares observed during the 2003 epoch (in black) and subsequent epochs (in red), plotted against stellar mass, stellar surface area, and SED IRAC slope. Corresponding legends present the τ coefficients and p -values obtained from Kendall's τ test. (e)–(f) Depiction of guiding trends: the peak plasma temperature and flare loop scale as functions of X-ray flare energy, based on the COUP flare sample and flare quantities from K. V. Getman et al. (2008a). The purple curves represent spline fits to the 25%, 50%, and 75% quartiles of the distributions, created using R's Constrained B-Splines `cobs` function (P. T. Ng & M. Maechler 2007).

These trends suggest that, for example, an X-ray superflare with an energy of $\log(E_{X,\text{fl}}) \sim 35$ erg exhibits median values and interquartile ranges (IQRs) for the flare peak plasma temperature and loop scale as follows: median $kT \sim 3.5$ keV, $\text{IQR}_{kT} \sim (2.7, 4.5)$ keV, median $L \sim 2.4 R_\odot$, and $\text{IQR}_L \sim (1.6, 3.5) R_\odot$. For an X-ray megafare with an energy of $\log(E_{X,\text{fl}}) \sim 36.5$ erg, these values are significantly higher: median $kT \sim 9$ keV, $\text{IQR}_{kT} \sim (6, 21)$ keV, median $L \sim 11 R_\odot$, and $\text{IQR}_L \sim (6, 20) R_\odot$. Note that the kT and L values could still be underestimated because the inferred X-ray flare energy values for the 2023 December flares often represent lower limits rather than true energy values.

Nevertheless, these estimates of flare quantities could prove valuable for comparison with empirical measurements of stellar magnetic field strengths from HPF, H^{13}CO^+ disk fluxes from ALMA, and CME radio fluxes from VLBA and for future modeling efforts involving magnetic dynamos, disks, and CMEs.

Out of 245 young X-ray-emitting stars, 81 exhibiting notable X-ray flares in 2023 December have been targeted by follow-up observations with VLBA, ALMA, or HET-HPF. Table 5 presents the properties of these 81 stars along with the inferred energetics of their X-ray flares. Among them, four stars (COUP 881, COUP 1333, COUP 1424, and COUP 1463) were observed with HET-HPF; four (COUP 414, COUP 561, COUP 1174, and COUP 1333) were observed with ALMA. A total of 80 out of 81 stars were observed using VLBA. Figure 5 presents a dozen examples of X-ray light curves for all the HET-HPF and ALMA targets, along with additional VLBA targets featuring some of the most powerful X-ray flares. Recall that detailed X-ray photon arrival diagrams and light curves for all the stars examined in this study are available in the electronic Figure Sets 2 and 3.

HET-HPF targets. HPF is demonstrated to be effective for Zeeman measurements. For instance, 0.8–1.7 kG stellar surface magnetic field strengths are readily seen in exposures of the $r = 14.1$ mag M7-type Teegarden’s Star. Similar detections were also made in Barnard’s Star (M4 type) and AD Leo (M3 type). All of them are from the broadening of the 1243 nm K I absorption line (R. C. Terrien et al. 2022). The detection of $B_{\text{spot}} = 10\text{--}20$ kG fields expected in Orion Nebula super- and megafaring stars (Section 1) should be achieved using the magnetic intensification technique relying on Ti lines at 960–980 nm with different magnetic sensitivity (O. Kochukhov 2021).

The strengths of Ti lines peak in late K- and M-type stars. Additionally, stars should be NIR-bright ($J < 11.5$ mag) to achieve a reasonable signal-to-noise ratio in the spectrum. Ensuring accurate measurements of magnetic strengths necessitates that the lines are not significantly broadened owing to stellar rotation or veiled by excess continuum emission owing to disk accretion. To adhere to these constraints, we selected four X-ray flaring stars (COUP 881, COUP 1333, COUP 1424, and COUP 1463) as targets for HPF observations.

All four are NIR-bright (with J magnitudes ranging from 10.8 to 11.5) stars of early M type with masses ranging from 0.6 to $0.9 M_\odot$. These stars demonstrate relatively slow rotation, with projected rotational velocities ranging from 9 to 14 km s^{-1} . Notably, two of these stars (COUP 1333 and COUP 1463) are surrounded by protoplanetary disks; however, they exhibit low accretion rates, as reported by K. V. Getman et al. (2005b). All of them are subject to low dust extinction, with A_V values not exceeding 2 mag, indicating their probable membership in the ONC cluster (E. D. Feigelson et al. 2005). Two stars (COUP 881, COUP 1463) exhibited exceptionally strong X-ray

superflares ($\log(E_{X,\text{fl}}) > 35.3$ erg), while the other two (COUP 1333, COUP 1424) generated even more powerful megafares ($\log(E_{X,\text{fl}}) > 36.1$ erg; see Figure 5).

ALMA targets. Our ALMA observations are focused on detecting and monitoring optically thin isotopologues of HCO^+ , such as H^{13}CO^+ and HC^{18}O^+ , to investigate the theoretically predicted temporal enhancements of HCO^+ resulting from the disk’s response to X-ray flares and changes in its chemistry (A. R. Waggoner et al. 2023).

The selection of ALMA targets was based on several criteria: previous detection of millimeter-band dust continuum emission to ensure the presence of massive protoplanetary disks, previous observations of gas emission indicating a high abundance of HCO^+ , minimal contamination from surrounding parental molecular cloud material, and visual source extinction below 15 mag to guarantee reliable spectral measurements.

The four ALMA targets selected, namely COUP 414, COUP 561, COUP 1174, and COUP 1333, exhibit a range of spectral types from early M type to G–K. They vary widely in terms of stellar properties, encompassing a broad spectrum of stellar mass (ranging from 0.5 to $3.6 M_\odot$), source extinction (ranging from 0 to 14 mag), and SED IRAC slope (ranging from -1.5 to 0.3). Of these targets, COUP 1333, exhibiting megafaring activity in X-rays, is the sole target observed by both HET-HPF and ALMA. In contrast, the remaining three ALMA targets showed more modest X-ray superflares, with \log X-ray energies ranging from 34.4 to 35.0 erg.

VLBA targets. Many of the 80 X-ray flaring stars observed by VLBA in 2023 December (Table 5) have been previously detected in radio surveys of the region (J. Forbrich et al. 2021). This prior detection enables precise alignment of source astrometry, facilitating the detection of potential shifts in the centroids of stars caused by X-ray flare-related CMEs moving away from the stars (Section 1).

These 80 stars exhibit a wide range of PMS stellar characteristics (Table 5). Estimates are available for 96% of their spectral types, 96% of their masses, 85% of their IRAC SED slopes, and 61% of their rotation quantities (either periods or projected rotation velocities). Regarding spectral types, 45% are classified as M-type stars, 46% as K-type stars, 5% as G-type stars, and 4% as B-type stars. The stellar masses in the sample range between 0.1 and $24 M_\odot$, with a median value of $0.9 M_\odot$. Similarly, stellar radii span from 1 to $8 R_\odot$, with a median value of $2.3 R_\odot$. Source extinctions range from 0 to 36 mag, with a median value of 4.6 mag. SED IRAC slopes span from -3.5 to 1.5, with a median value of -1.5 . Time-averaged COUP X-ray luminosities span from $8.7 \times 10^{28} \text{ erg s}^{-1}$ to $5.7 \times 10^{31} \text{ erg s}^{-1}$, with a median value of $1.8 \times 10^{30} \text{ erg s}^{-1}$. The energies of the large X-ray flares range from $6.5 \times 10^{33} \text{ erg}$ to $8.4 \times 10^{36} \text{ erg}$, with a median value of $2.4 \times 10^{35} \text{ erg}$.

Figure 5 showcases five among the most powerful X-ray megafares with $\log(E_X) > 36$ erg produced by the VLBA target stars COUP 539, COUP 871, COUP 939, COUP 1333, and COUP 1424. The apparent durations of these extraordinary flares easily exceed 100 ks, and the apparent amplitudes (as ratios of the flare peak X-ray luminosity to the characteristic X-ray luminosity) exceed a factor of 9 for all of these flares and a factor of 40 for three of them.

5.3. Search for Signs of Magnetic Cyclic Activity

Figures 6(a)–(c) display the comparison of stellar X-ray characteristic luminosities across different epochs. The unity

Table 5
VLBA, ALMA, and HET-HPF Targets Observed in 2023 December

Src.	$\log(E_{X,\text{fl}})$ (erg)	$\sigma_{\log(E_{X,\text{fl}})}$ (erg)	SpT	A_V (mag)	M (M_\odot)	R (R_\odot)	α_{IRAC}	P_{rot} (days)	$v_{\text{rot}} \sin(i)$ (km s $^{-1}$)	ME (keV)	$\log(L_X)$ (erg s $^{-1}$)
(1)	(2)	(3)	(4)	(5)	(6)	(7)	(8)	(9)	(10)	(11)	(12)
COUP939	36.93	0.007	K8e	10.8	3.0	4.7	−0.3	1.8	30.9
COUP1035	36.30	0.022	...	18.5	3.0	4.9	−1.9	2.3	31.1
COUP1333	36.27	0.008	em, M0.5	1.1	0.8	2.2	−0.9	9.0	13.8	1.2	30.1
COUP621	36.25	0.024	...	35.6	22.6	6.1	3.6	30.9
COUP1298	36.16	0.023	...	28.2	2.2	4.9	−0.5	3.4	29.7
COUP871	36.12	0.011	M0.5	3.4	0.8	1.5	8.3	1.5	30.3
COUP1424	36.11	0.011	M1	2.1	0.9	1.9	−2.8	10.6	12.2	1.3	30.3
COUP539	36.07	0.036	4.0	30.2
COUP262	35.95	0.020	K5	11.4	3.0	4.7	−2.6	3.8	27.5	1.9	31.1
COUP444	35.92	0.028	...	28.2	0.5	2.5	−1.0	3.0	30.1
COUP403	35.91	0.022	K?, M2.7	2.8	0.3	2.3	−0.3	3.2	30.1
COUP43	35.88	0.014	M1	2.1	0.9	2.2	−2.5	...	70.6	1.3	30.3

Note. A subset of 81 stars exhibiting prominent X-ray flares in 2023 December and observed with either VLBA, ALMA, or HET-HPF. The COUP 881, COUP 1333, COUP 1424, and COUP 1463 stars have been observed by HET-HPF. The COUP 414, COUP 561, COUP 1174, and COUP 1333 have been observed by ALMA. And all but one (COUP 561) of the stars listed in this table have been observed by VLBA. These targets are listed in descending order of their X-ray flare energy values. Examples of table entries are provided here; the full machine-readable table for all 81 young stars is available in the electronic edition of this paper. Column (1): source name. Columns (2)–(3): energy values of large X-ray flares detected in 2023 December (from Table 4). Columns (4)–(12): stellar properties, including spectral type, source’s visual extinction, stellar mass and radius, SED IRAC slope, stellar rotation period and projected velocity, X-ray ME, and time-averaged X-ray luminosity (all from Table 2).

(This table is available in its entirety in machine-readable form in the [online article](#).)

line falls within the confidence intervals of the model fits for all multi-epoch comparisons. These multi-epoch bivariate distributions exhibit no biases and IQR dispersions of 0.4 dex. The lack of strong biases indicates that our X-ray data analyses are accurate.

For each star, we calculate a simple χ^2 statistic to measure the deviation of its characteristic X-ray luminosities for each available epoch ($L_{X,\text{char},i}$) from the characteristic luminosity averaged across all epochs ($\langle L_{X,\text{char}} \rangle$), considering the uncertainties associated with each epoch i , $\epsilon L_{X,\text{char},i}$:

$$\chi^2 = \sum_{i=1}^4 \left(\frac{(L_{X,\text{char},i} - \langle L_{X,\text{char}} \rangle)^2}{\epsilon L_{X,\text{char},i}^2} \right). \quad (1)$$

We also compute the amplitude of the long-term variations in the X-ray characteristic luminosity as

$$A = \frac{\max(L_{X,\text{char}}) - \min(L_{X,\text{char}})}{\min(L_{X,\text{char}})}. \quad (2)$$

From the plot of A as a function of χ^2 (Figure 6(d)), we select 15 stars with the highest statistically reliable amplitudes (red points). These stars are COUP 315, COUP 403, COUP 444, COUP 504, COUP 536, COUP 539, COUP 599, COUP 621, COUP 801, COUP 823, COUP 901, COUP 997, COUP 1054, COUP 1139, and COUP 1298. Figure 6(e) indicates that the amplitudes A of the full PMS stellar sample do not correlate with stellar mass or rotation (the latter graph is not shown). However, we observe a marginally statistically significant correlation with the indicator of disks (Figure 6(f)), and the sample of 15 stars with the highest amplitudes (Figure 6(d)) primarily comprises disk-bearing stars (except for COUP 997). Their source extinctions are generally systematically higher than those of the entire 245-star sample (graph is not shown). The presence of disks suggests that their long-term variability may not stem from magnetic cyclic activity but rather, possibly,

from long-term variations in accretion columns (A. M. Cody et al. 2022). These accretion columns are expected to attenuate stellar X-ray emission, due to either the presence of dense, cold, non-X-ray-emitting gas or additional gas absorption within these columns (T. Preibisch et al. 2005).

To mitigate possible long-term effects of disks and accretion, our subsequent step involved analyzing a subset of stars consisting only of those without disks (Figures 6(g)–(i)). Within this subset, we observed that the X-ray characteristic variability amplitudes exhibited no correlations with either stellar mass or rotation. Among them, nine stars (highlighted in green) demonstrated statistically reliable, highest X-ray characteristic variability amplitudes (see Table 6). Among these, one system, COUP 1232, is a high-mass hierarchical triple (B. Stelzer et al. 2005). In such a case, the characteristic variability may be unrelated to magnetic cyclic activity. The remaining eight stars require further analysis utilizing extended archival Chandra ACIS-HETG data, a task that lies beyond the scope of the current paper.

In our analysis, considering the uncertainties associated with their amplitudes A , we observe that the majority of PMS stars display X-ray characteristic variability amplitudes below 1.5. This variation is notably smaller than the factor of >10 difference seen between the maximum and minimum X-ray activity levels on the current Sun, attributed to its 11 yr cyclic activity (P. G. Judge et al. 2004).

For the sample of 87 diskless PMS stars shown in Figure 6(g), we performed simulations to derive the CDFs of their apparent X-ray variability amplitude A_{app} . These simulations were conducted with various assumptions about the intrinsic cyclical activity periods (P_{cyc}) and intrinsic cyclical amplitudes (A_{intr}). Each star’s X-ray cyclical activity was modeled with a sinusoidal pattern and a random phase. The simulated stars were observed four times, with observation gaps reflecting the actual gaps between the four observation epochs listed in Table 1. Simulations covered a broad range of

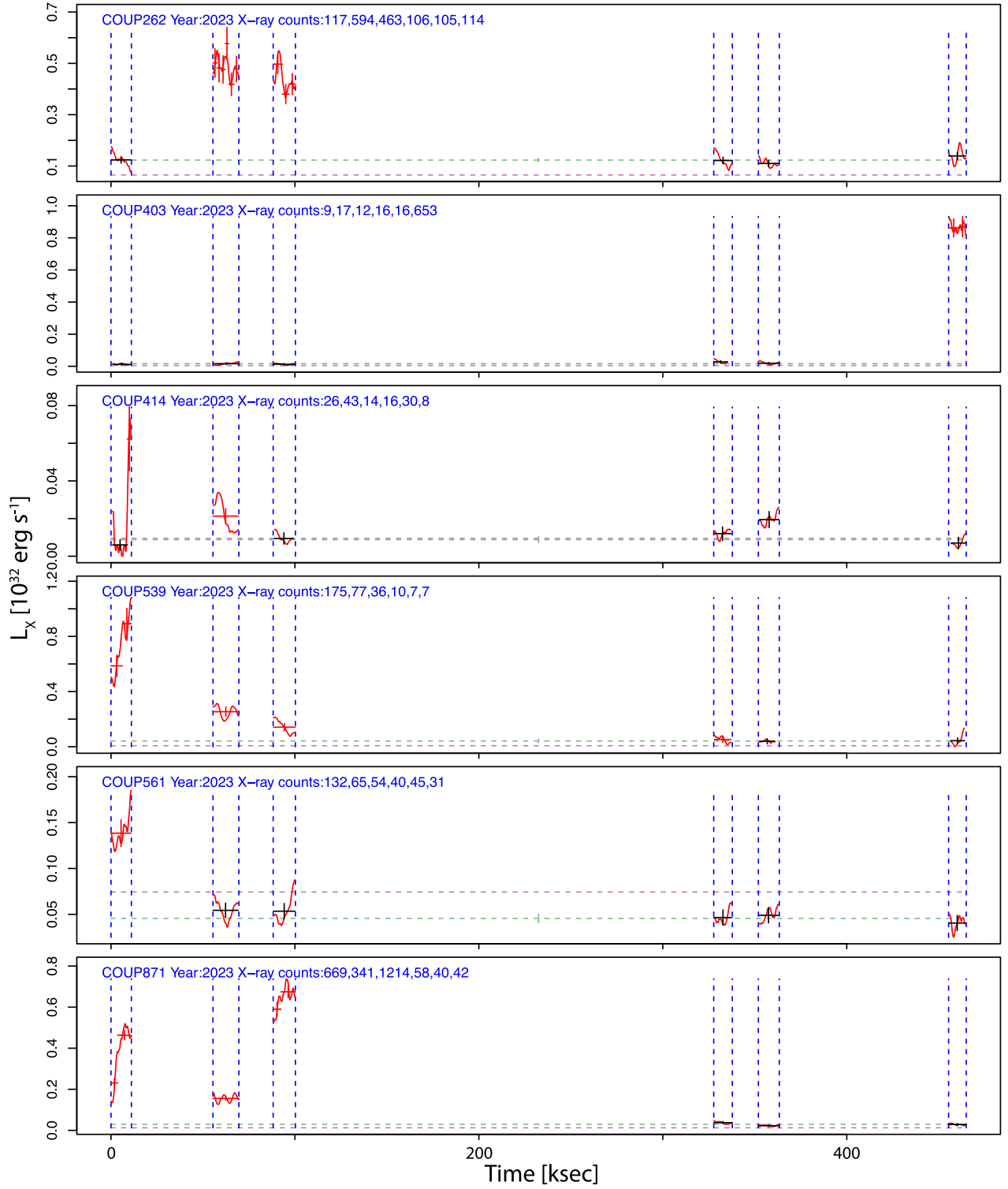


Figure 5. Examples of X-ray light curves presented in units of intrinsic stellar X-ray luminosity for select targets observed with HET-HPF, ALMA, and VLBA. For further details, consult the caption of Figure 3. Refer to the next page for the continuation of the figure.

A_{intr} and three different P_{cyc} values (1, 5, and 10 yr). The real observed empirical cumulative distribution function (ECDF) of A (shown in Figure 6(g)) was compared to the simulated CDFs of A_{app} using the AD test to infer the properties of the intrinsic cyclical activity of our 87 diskless stars.

The simulations indicate that an intrinsic cyclical activity amplitude of $A_{\text{intr}} = 1.7$, regardless of P_{cyc} , best matches the observed pattern of A . Figure 7 shows typical instances of A_{app}

CDFs from simulations with $A_{\text{intr}} = 1.7$ and P_{cyc} values of 1, 5, and 10 yr. Solutions with intrinsic amplitudes lower (higher) than 1.7 (not shown in the graph) would systematically fall to the left (right) of the observed A locus.

Observed cases with $A > 1.6$, which represent less than 20% of our stellar sample, deviate from the simulation outcomes (Figure 7). For some of these cases, with $\log(\chi^2) < 2$ and large error bars on A (Figure 6(g)), the A estimates may be highly

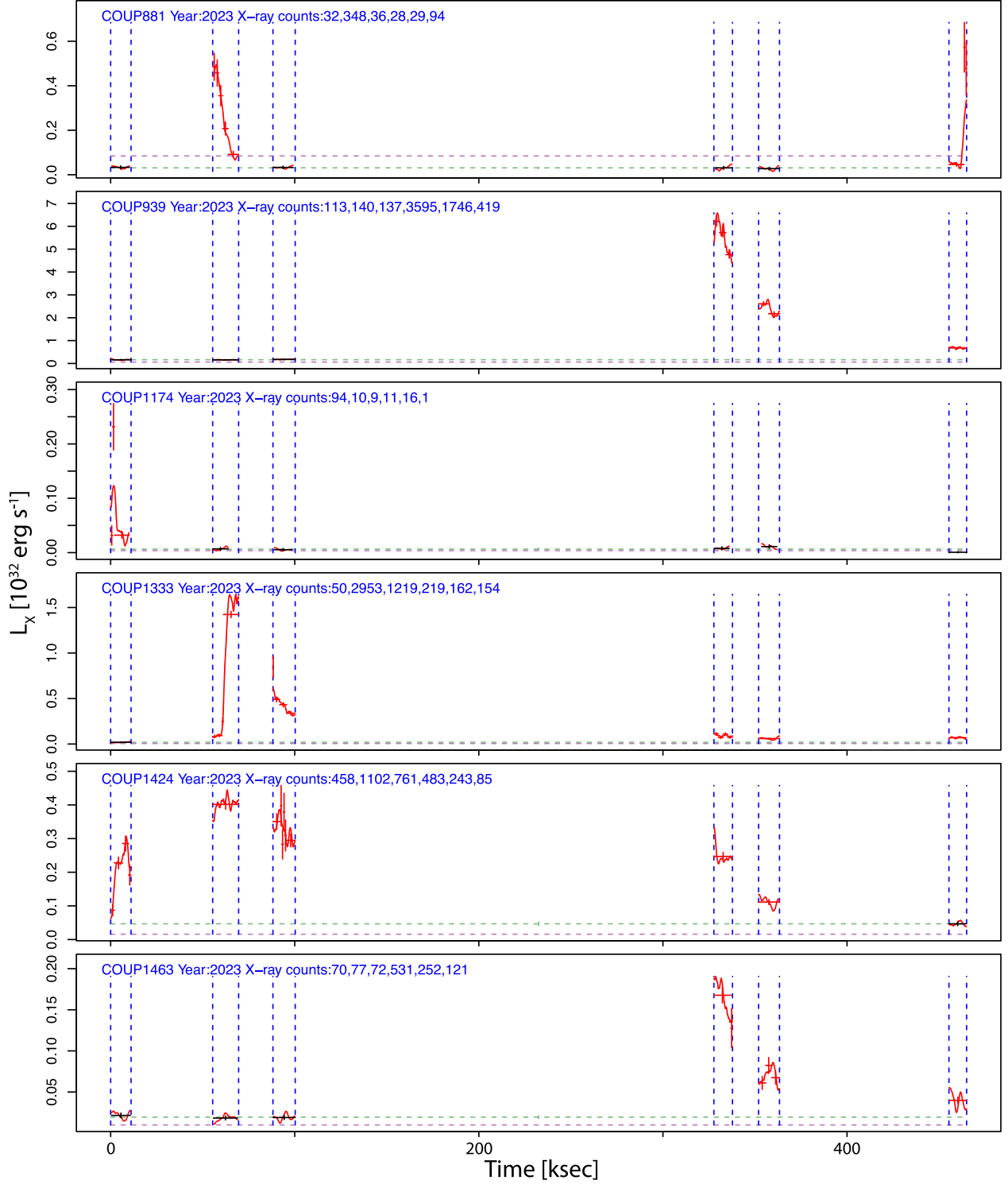


Figure 5. (Continued.)

uncertain. For the remaining nine stars with the highest reliable A values, listed in Table 6 and considered good candidates for future cyclic activity analyses, their intrinsic A_{intr} may be systematically higher than the lower value of $A_{\text{intr}} = 1.7$ that fits the majority of our sample.

The diminished levels of long-term X-ray characteristic variability in most of our PMS stars align with the concept that young, fully convective stars possess saturated α^2 magnetic

dynamoes, which operate independently of rotation (A. Reiners et al. 2022). Additionally, the presence of extensive surface coverage of coronal active regions and extremely elongated X-ray coronal structures (M. Coffaro et al. 2022; K. V. Getman et al. 2022; K. V. Getman et al. 2023) contributes to this observation. While PMS magnetic cycling is theoretically predicted (C. Emeriau-Viard & A. S. Brun 2017), the existence of saturated X-ray coronal structures might mitigate the

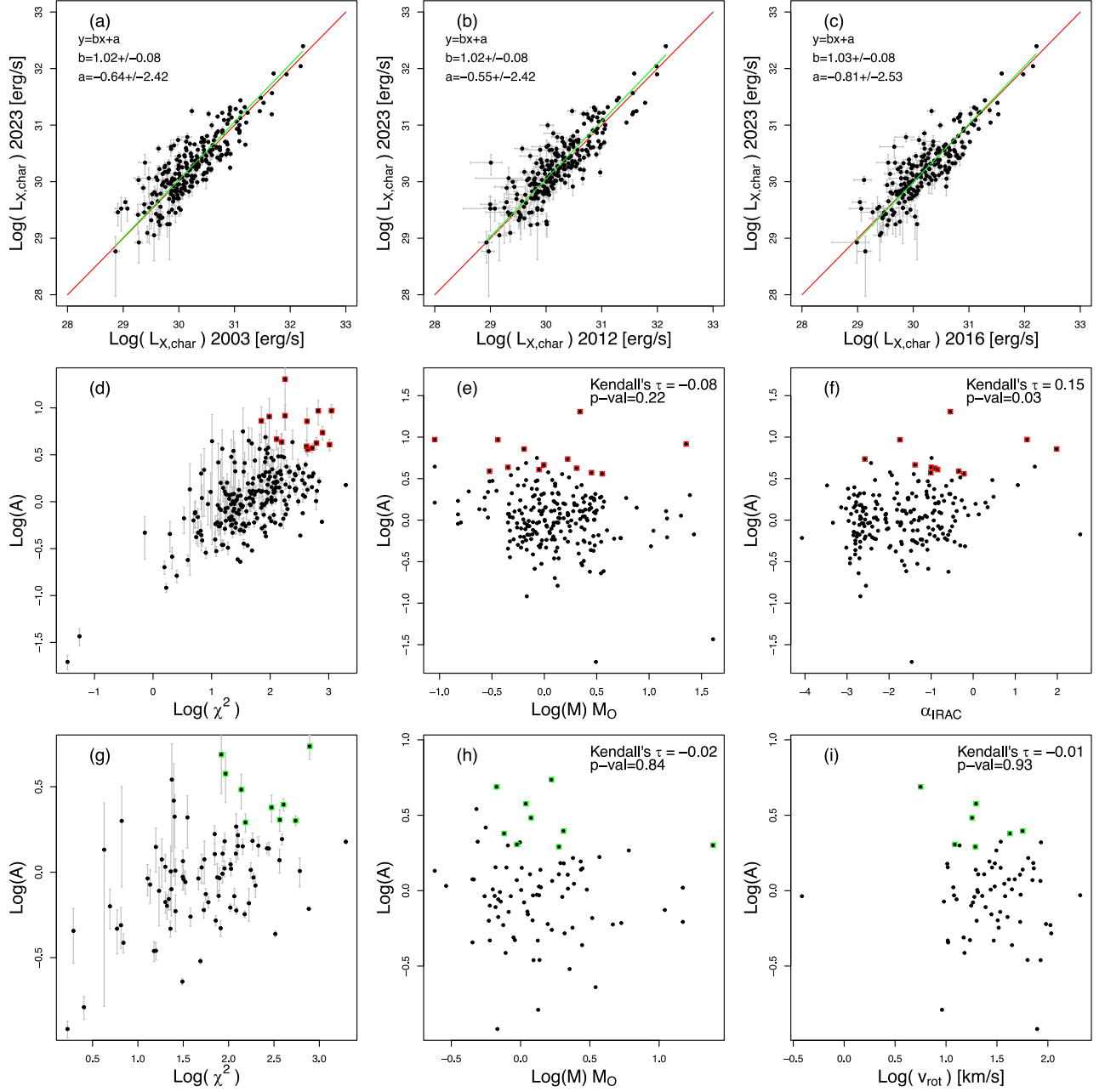


Figure 6. (a)–(c) Comparison of stellar X-ray characteristic luminosities across different epochs. The unity lines are depicted in red. Linear regression fits using the Major Axis algorithm within R’s `lmodel2` function are shown in green. Figure legends list the intercept, slope, and half-widths of the 95% confidence intervals inferred by `lmodel2`. (d)–(f) Long-term X-ray characteristic variability amplitude (A) plotted against χ^2 , stellar mass, and SED IRAC slope for the entire stellar sample. Stars with the highest statistically reliable A are highlighted with red points. Figure legends provide coefficients and p -values from Kendall’s τ test. (g)–(i) Similar to panels (d)–(f), but for the subset of diskless stars. Diskless stars with the highest statistically reliable A are denoted with green points. (i) For diskless stars, amplitude A plotted against stellar rotation velocity.

observable manifestation of PMS dynamo cycling. Furthermore, the presence of a saturated α^2 dynamo could potentially inhibit strong magnetic cycling altogether.

5.4. Do All PMS Stars Produce Megafares?

An important question regarding disk and planetary irradiation is whether powerful flares occur in only a subset of PMS stars or the entire population produces megafares. Previous studies on powerful PMS flares (e.g., F. Favata et al. 2005; S. J. Wolk et al. 2005; M. Caramazza et al. 2007; J. F. Colombo et al. 2007; B. Stelzer et al. 2007; K. V. Getman et al. 2008a;

E. Flaccomio et al. 2018; K. V. Getman & E. D. Feigelson 2021) have been unable to address this question because the recurrence timescale of megafares is often longer than typical X-ray observation exposure times. However, we can examine this issue here, where over 200 stars exhibited flares in certain Chandra exposures spanning two decades (see Table 1).

Ignoring the massive COUP 809 and COUP 1232 stars (O-type Theta Ori 1C and Theta² Ori A), we consider here a subsample of 222 stars, for which X-ray flares are registered in at least one of the COUP (i.e., epoch 2003 observations) observations (Table 4). In this sample, 80 stars exhibited megafares during the lengthy COUP observation in 2003 (see

Table 6
Candidates for Future Cyclic Activity Analyses

Src.	χ^2	A	σ_A	SpT	A_V (mag)	M (M_\odot)	R (R_\odot)	α_{IRAC}	P_{rot} (days)	$v_{\text{rot}} \sin(i)$ (km s^{-1})	ME (keV)	$\log(L_X)$ (erg s^{-1})
(1)	(2)	(3)	(4)	(5)	(6)	(7)	(8)	(9)	(10)	(11)	(12)	(13)
COUP997	783.2	5.4	0.9	K8	4.6	1.7	2.2	−2.6	1.5	30.8
COUP1087	403.4	2.5	0.2	G/K	3.0	2.0	3.3	−2.8	...	56.5	1.3	31.4
COUP1127	137.7	3.0	0.7	K7:	4.5	1.2	1.9	−2.3	7.2	18.0	1.5	30.4
COUP1151	153.2	1.9	0.2	K6	3.5	1.9	3.2	−2.7	11.5	19.4	1.3	30.8
COUP1210	92.5	3.8	1.2	K2/4	5.5	1.1	2.5	−2.0	...	19.7	1.6	30.5
COUP1232	547.7	2.0	0.1	B1:V	2.5	24.5	7.9	−2.4	0.9	31.8
COUP1355	83.2	4.9	2.0	M3.5	0.0	0.7	1.3	−2.4	10.4	5.6	1.2	30.1
COUP1424	366.1	2.0	0.3	M1	2.1	0.9	1.9	−2.8	10.6	12.2	1.3	30.3
COUP1516	297.5	2.4	0.4	K1/4	0.0	0.8	1.4	−3.0	...	42.4	1.1	30.2

Note. A subset of nine diskless PMS stars exhibiting the highest statistically reliable amplitudes of long-term X-ray characteristic variations (green points in Figures 6(g)–(i)). Column (1): source name. Columns (2)–(4): χ^2 , amplitude of variation, and its 1σ uncertainty. Columns (5)–(13): stellar properties, including spectral type, source’s visual extinction, stellar mass and radius, SED IRAC slope, stellar rotation period and projected velocity, X-ray ME, and time-averaged X-ray luminosity (all from Table 2).

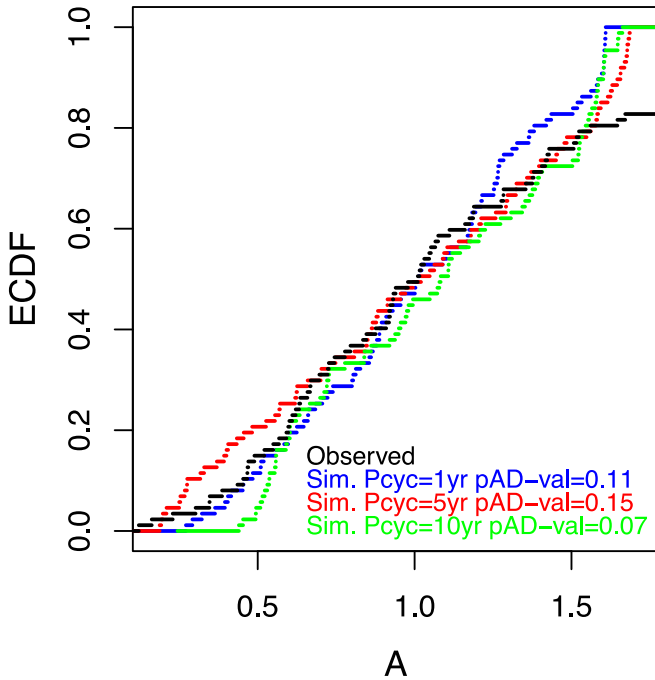


Figure 7. Comparison of the observed X-ray characteristic variability amplitude A (black) for our sample of 87 diskless PMS stars (shown in Figure 6(g)), with the A_{app} results from simulations (described in the text) assuming intrinsic cyclic activity periods of 1 yr (blue), 5 yr (red), and 10 yr (green) and an intrinsic variability amplitude $A_{\text{intr}} = 1.7$. The p -values from the AD test for these comparisons are provided in the figure legend.

Column “Early Megaflares Y” in Table 7), five megaflared in 2012, five megaflared in 2016, and eight megaflared in 2023 (see Row “Later Megaflares Y” in Table 7). The last 18 stars were all different, that is, no star exhibited a megaflare twice in the 2012–2016–2023 epochs. By itself, this does not suggest that megaflaring is restricted to a small fraction of ONC stars. Nine of these 18 stars also showed megaflaring in the early COUP data (see the first cell with Column “Early Megaflares Y” and Row “Later Megaflares Y” in Table 7).

The question can be quantitatively examined using a 2×2 contingency table that compares the (non)flaring stars from the early COUP observation with the (non)flaring stars from the

Table 7
Megaflaring Stars in COUP versus Later Epochs

		Early Megaflares		Totals
		Y	N	
Later	Y	9	9	18
Megaflares	N	71	133	204
Totals		80	142	222

later epochs (Table 7). Using the Fisher exact test for count data, the probability that a correlation exists between the occurrence of early and later megaflares is $p \simeq 0.2$.¹⁵ This test would be significant with $p < 0.01$ if only ≥ 12 of the 18 late flaring stars were also early flaring stars. There is thus no statistical evidence that the megaflares repeatedly occur in the same subsample of Orion Nebula stars.

But we must recognize that the majority ($133/222 = 60\%$ in Table 7) of stars examined here did not exhibit megaflares in any epoch, and most stars are too faint to appear at all in the shorter later exposures. There are two plausible explanations for this: (a) the exposures were not long enough and these stars would produce megaflares if we looked long enough with Chandra (K. V. Getman & E. D. Feigelson 2021), or (b) these stars would never megaflare, so the incidence of megaflaring is bimodal. However, a continuous unimodal population of flaring stars is suggested by the comparison of early and late flare energies in Figures 4 and 8. Early and late flare energies are associated with each other with a p -value of 0.002, indicating statistical significance according to the nonparametric Kendall’s τ correlation test, which is astrophysically attributed to the underlying correlation between flare energy and stellar mass/size (Section 5.1). Again, as with Table 7, there is no indication that the megaflaring stars represent a special subpopulation of PMS stars.

Our findings suggest that all fully convective PMS stars produce extremely powerful X-ray flares. A solar-mass PMS star is expected to generate a few megaflares per year

¹⁵ The Fisher exact test give probabilities of class differences in 2×2 contingency tables when counts are small (A. Agresti 2006). Software implementations include `fisher.test` in R and `scipy.stats.fisher_exact` in Python.

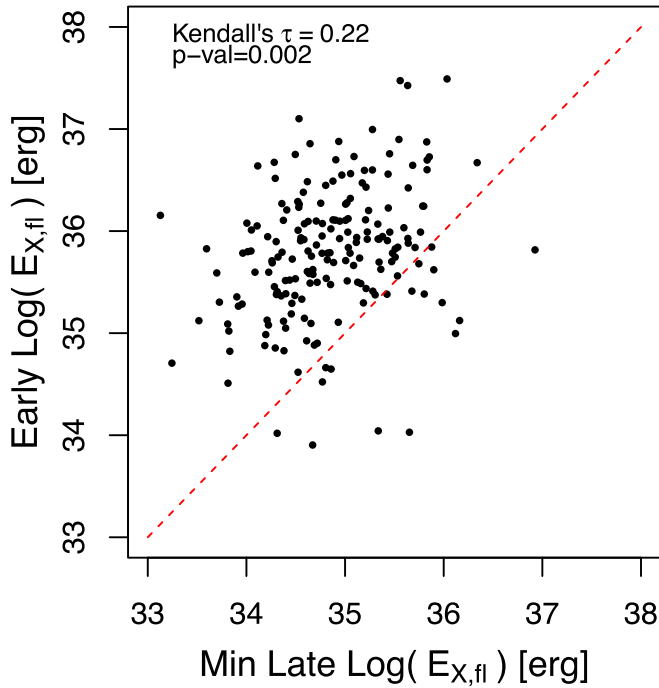


Figure 8. Bivariate relationship between early (epoch 2003) and late (epochs 2012, 2016, and 2023) flares for Orion Nebula PMS stars. If multiple flares are seen in more than one later epoch, the weaker flare is shown. The dashed red line shows equal luminosities in early and late epochs.

(K. V. Getman & E. D. Feigelson 2021). This would mean that every protoplanetary disk and, when they are dissipated (A. J. W. Richert et al. 2018), every nascent primordial planetary atmosphere is subject to millions of violent stellar magnetic reconnection events, possibly including powerful CMEs (Section 1).

6. Conclusions

This study constitutes an important component of a comprehensive, multi-telescope effort aimed at exploring various aspects of PMS X-ray emission. In 2023 December, we conducted nearly simultaneous observations utilizing the Chandra, HET, ALMA, and VLBA telescopes, targeting the PMS stellar members within the Orion Nebula star-forming region. Additionally, we analyzed archival Chandra data spanning previous epochs in 2003, 2012, and 2016. Leveraging this rich data set, our project is poised to achieve several key scientific objectives (Section 1), including the assessment of PMS surface magnetic field strengths following a large X-ray flare through synergistic HET-HPF/Chandra observations, exploration of X-ray flare impacts on disk chemistry via ALMA/Chandra investigations, hunting for flare-associated CMEs through VLBA/Chandra observations, and scrutiny of the multi-epoch behaviors of both PMS X-ray characteristic (baseline) and flare emission utilizing Chandra data.

Our careful analysis of the multi-epoch Chandra data, making use of CIAO and AE tools, led to the extraction and X-ray photometric characterization of over 800 young stellar members of the Orion Nebula (Section 2). Among these, we identified 245 stars as the brightest in the 2023 epoch and compiled lists of their stellar properties (Table 2). Additionally, we generated atlases of stellar X-ray photon arrival diagrams and light curves (Figure Sets 2 and 3), identified significant flare and baseline segments, and computed the intrinsic X-ray

luminosity levels and energetics associated with these segments (Section 4).

In Section 5.1, we observe a robust positive correlation between the X-ray energies of PMS flares identified across multiple epochs and the stellar mass and size. This correlation is attributed to the positive dependence of the underlying convection-driven dynamo on the stellar volume. Notably, flare energies do not exhibit a dependency on the presence or absence of protoplanetary disks. This suggests that the solar-type flare mechanism, involving both X-ray loop footpoints anchored in the stellar surface, is operational in PMS stars. While similar results have been reported previously for flares with $\log(E_{X,fl}) > 35$ erg, our current findings represent the first empirical observation of such trends in numerous less powerful PMS flares.

In Section 5.2, we analyze 81 X-ray flaring stars selected as targets for our subsequent observations with HET, ALMA, and VLBA. We meticulously examine their stellar properties alongside the characteristics of their prominent X-ray flares, offering comprehensive insights. These details are tabulated, serving as crucial supplementary material for our ongoing analyses and forthcoming HET-HPF, ALMA, and VLBA papers.

In Section 5.3, we observe that the majority of the analyzed PMS stars exhibit relatively minor long-term variations in their baseline X-ray emission. This suggests that either convection-driven dynamos, operating within these rapidly rotating stars, do not generate magnetic cycles or the PMS X-ray emission originating from coronal structures—potentially saturated across extensive stellar coronal volumes—diminishes the manifestation of dynamo cycling. We compile a list of several diskless stars that display the highest multi-epoch baseline variations. Constituting only a small fraction of our entire stellar sample, these stars are considered prime candidates for future investigations into PMS magnetic dynamo cycles using additional extended archival Chandra ACIS-HETG data.

In Section 5.4, we discover that X-ray megaflaring is ubiquitous and not limited to a specific subset of stars. This indicates that every protoplanetary disk—and upon their dissipation, every emerging primordial planetary atmosphere—is subjected to millions of intense stellar magnetic reconnection events, potentially including powerful CMEs.

In the Appendix, we evaluate the temporal increase in the apparent Chandra X-ray MEs of young Orion Nebula stars due to Chandra’s sensitivity degradation.

Acknowledgments

We are grateful to the anonymous referee for providing thoughtful and helpful comments that improved the manuscript. We thank the Chandra Mission Operations group for scheduling the X-ray observations for 2023 December. We thank Patrick Broos (Penn State) for his valuable consultations regarding the use of the ACIS Extract software package. This project is supported by the SAO Chandra grant GO3-24010X (PI: K. Getman) and the Chandra ACIS Team contract SV4-74018 (PIs: G. Garmire & E. Feigelson), issued by the Chandra X-ray Center, which is operated by the Smithsonian Astrophysical Observatory for and on behalf of NASA under contract NAS8-03060. The Chandra Guaranteed Time Observations (GTO) data used here and listed in K. V. Getman et al. (2005b) were selected by the ACIS Instrument Principal Investigator, Gordon P. Garmire, of the Huntingdon Institute for X-ray Astronomy, LLC, which is under contract to the

Smithsonian Astrophysical Observatory; contract SV2-82024. O.K. acknowledges support by the Swedish Research Council (grant agreement Nos. 2019-03548 and 2023-03667). Support for C.J.L. was provided by NASA through the NASA Hubble Fellowship grant No. HST-HF2-51535.001-A awarded by the Space Telescope Science Institute, which is operated by the Association of Universities for Research in Astronomy, Inc., for NASA, under contract NAS5-26555. S.A.D. acknowledges the M2FINDERS project from the European Research Council (ERC) under the European Union’s Horizon 2020 research and innovation program (grant No. 101018682). This paper employs a list of Chandra data sets, obtained by the Chandra X-ray Observatory, contained in DOI:[10.25574/cdc.285](https://doi.org/10.25574/cdc.285).

Facility: CXO

Software: R (R Core Team 2020), HEASOFT (Nasa High Energy Astrophysics Science Archive Research Center (Heasarc) 2014), CIAO (A. Fruscione et al. 2006), AE (P. S. Broos et al. 2010; P. Broos et al. 2012)

Appendix

Temporal Increase in Apparent Chandra X-Ray Median Energy due to Sensitivity Degradation

We assess the temporal evolution of the Chandra ACIS-I apparent X-ray MEs for young stars in the Orion Nebula. These changes are primarily attributed to the accumulation of contamination on the optical blocking filters. The presented calculations may serve as a valuable resource for future researchers examining the Chandra archives.

Figure 9 compares ME values across multiple epochs, accounting for various sets of X-ray light-curve segments from Table 3 and different energy ranges. Figures 9(a)–(f) confirm

the expected linear trends between the X-ray ME measured in 2003 and the MEs measured in the other three epochs, with systematically higher linear fit intercept values observed in the older epochs owing to decreased Chandra sensitivity. However, the trends are primarily influenced by the much more numerous X-ray softer stars.

Figures 9(g)–(i) and Table 8 offer a clearer representation of the actual distributions of ME changes across different epochs, energy ranges, and selections of light-curve segments.

Since large flares tend to produce a higher fraction of hard X-ray photons and the longer 2003 Chandra exposure captures more large flares, the value of the fractional ME, $(ME_{\text{epoch}} - ME_{2003})/ME_{2003}$, may be influenced by flares. The exclusive choice of characteristic light-curve segments mitigates such potential effects. Indeed, Figures 9(g) and (h) indicate small systematic differences between the fractional MEs for the same epoch, as shown by the shifts between the solid curves (using only characteristic light-curve segments) and dashed curves (using all light-curve segments) for epochs 2012 and 2016. This suggests that for evaluating Chandra instrumental effects it may be preferable to rely on results obtained from the selection of exclusively characteristic light-curve segments.

The effects of instrumental sensitivity are significantly more pronounced in softer ME ranges ($ME_{2003} < 3$ keV) compared to harder ranges ($ME_{2003} \geq 3$ keV). For example, when examining the ME fractional difference between epochs 2023 and 2003, the 50th and 75th percentiles of the difference distributions in softer energy ranges are 29% and 42%, respectively. In contrast, for harder energy ranges, these quantities are only 3% and 7%, respectively (Table 8).

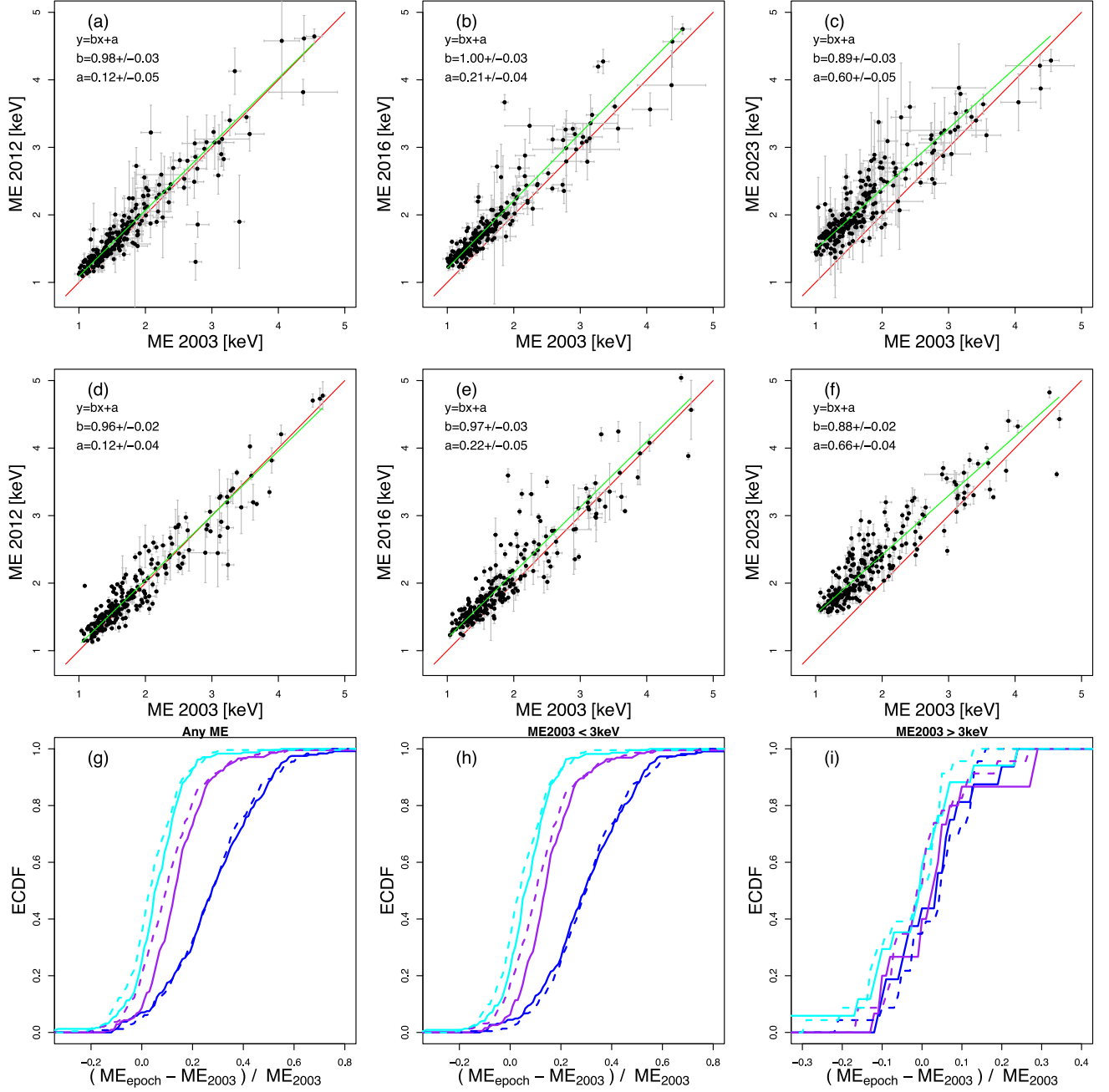













Figure 9. (a)–(f) Comparison of Chandra ACIS-I apparent X-ray MEs across different epochs. The red lines represent the unity reference, while the green lines show linear regression fits derived using the Major Axis algorithm, which treats variables symmetrically (D. I. Warton et al. 2006), from R’s `lmodel2` function (P. Legendre & L. Legendre 1998). The figure legends display the intercept, slope, and 68% confidence interval half-widths from the `lmodel2` results. Panels (a)–(c) include only characteristic light-curve segments (i.e., “c” in Column (9) of Table 3), while panels (d)–(f) encompass all light-curve segments (i.e., large flares “f,” mild variability “n,” and characteristic “c”). (g–i) ECDFs of fractional differences $(ME_{\text{epoch}} - ME_{2003}) / ME_{2003}$ across different energy ranges, epochs, and light-curve segments. Energy ranges: (g) all stars, (h) stars with $ME_{2003} < 3$ keV, and (i) stars with $ME_{2003} \geq 3$ keV. Epochs: 2012 (cyan), 2016 (purple), and 2023 (blue). Light-curve segments: solid curves represent only characteristic segments, while dashed curves represent all segments.

Table 8
Chandra ACIS-I ME Changes

Frac. Difference (1)	Light-curve Segments (2)	Energy Range (3)	25% (4)	50% (5)	75% (6)	Intercept (7)	Slope (8)	<i>p</i> -value (9)
$(ME_{2012} - ME_{2003})/ME_{2003}$	Char	Any ME	0.00	0.05	0.12	0.12 ± 0.05	0.98 ± 0.03	0.001
$(ME_{2016} - ME_{2003})/ME_{2003}$	Char	Any ME	0.06	0.13	0.20	0.21 ± 0.04	1.00 ± 0.03	0.001
$(ME_{2023} - ME_{2003})/ME_{2003}$	Char	Any ME	0.16	0.28	0.40	0.60 ± 0.05	0.89 ± 0.03	0.001
$(ME_{2012} - ME_{2003})/ME_{2003}$	All	Any ME	-0.02	0.03	0.10	0.12 ± 0.04	0.96 ± 0.02	0.001
$(ME_{2016} - ME_{2003})/ME_{2003}$	All	Any ME	0.01	0.10	0.18	0.22 ± 0.05	0.97 ± 0.03	0.001
$(ME_{2023} - ME_{2003})/ME_{2003}$	All	Any ME	0.16	0.28	0.39	0.66 ± 0.04	0.88 ± 0.02	0.001
$(ME_{2012} - ME_{2003})/ME_{2003}$	Char	$ME_{2003} < 3 \text{ keV}$	0.01	0.06	0.12	0.05 ± 0.06	1.02 ± 0.04	0.001
$(ME_{2016} - ME_{2003})/ME_{2003}$	Char	$ME_{2003} < 3 \text{ keV}$	0.07	0.13	0.21	0.08 ± 0.06	1.09 ± 0.04	0.001
$(ME_{2023} - ME_{2003})/ME_{2003}$	Char	$ME_{2003} < 3 \text{ keV}$	0.20	0.29	0.42	0.35 ± 0.08	1.05 ± 0.05	0.001
$(ME_{2012} - ME_{2003})/ME_{2003}$	All	$ME_{2003} < 3 \text{ keV}$	-0.02	0.04	0.12	0.07 ± 0.05	1.00 ± 0.03	0.001
$(ME_{2016} - ME_{2003})/ME_{2003}$	All	$ME_{2003} < 3 \text{ keV}$	0.03	0.10	0.18	0.02 ± 0.08	1.10 ± 0.05	0.001
$(ME_{2023} - ME_{2003})/ME_{2003}$	All	$ME_{2003} < 3 \text{ keV}$	0.20	0.30	0.41	0.40 ± 0.08	1.05 ± 0.05	0.001
$(ME_{2012} - ME_{2003})/ME_{2003}$	Char	$ME_{2003} \geq 3 \text{ keV}$	-0.10	-0.01	0.04	-2.45 ± 1.85	1.67 ± 0.53	0.003
$(ME_{2016} - ME_{2003})/ME_{2003}$	Char	$ME_{2003} \geq 3 \text{ keV}$	-0.04	0.02	0.05	-0.38 ± 1.31	1.14 ± 0.37	0.004
$(ME_{2023} - ME_{2003})/ME_{2003}$	Char	$ME_{2003} \geq 3 \text{ keV}$	-0.05	0.03	0.07	1.32 ± 0.63	0.64 ± 0.18	0.004
$(ME_{2012} - ME_{2003})/ME_{2003}$	All	$ME_{2003} \geq 3 \text{ keV}$	-0.12	0.00	0.03	-1.71 ± 0.70	1.44 ± 0.20	0.001
$(ME_{2016} - ME_{2003})/ME_{2003}$	All	$ME_{2003} \geq 3 \text{ keV}$	-0.07	-0.01	0.03	-0.67 ± 0.92	1.18 ± 0.26	0.001
$(ME_{2023} - ME_{2003})/ME_{2003}$	All	$ME_{2003} \geq 3 \text{ keV}$	-0.02	0.05	0.10	0.35 ± 0.76	0.92 ± 0.21	0.001

Note. Table of the 25th, 50th, and 75th percentiles of the ME fractional difference distributions (as illustrated in Figures 9(g)–(i)), along with the `lmodel2` fit results for the ME_{epoch} versus ME_{2003} relationships (as shown in Figures 9(a)–(f)). Column (1): form of fractional difference. Column (2): X-ray source light-curve segments included in the calculations. Column (3): energy range. Columns (4)–(6): inferred 25th, 50th, and 75th percentiles of the distributions. Columns (7)–(9): results from linear regression fits using `lmodel2`, including the intercept, slope, and *p*-value testing the null hypothesis of no relationship. All *p*-values are small, indicating statistically significant relationships between ME_{epoch} and ME_{2003} .

ORCID iDs

Konstantin V. Getman  <https://orcid.org/0000-0002-6137-8280>
 Eric D. Feigelson  <https://orcid.org/0000-0002-5077-6734>
 Abygail R. Waggoner  <https://orcid.org/0000-0002-1566-389X>
 L. Ilse-dore Cleeves  <https://orcid.org/0000-0003-2076-8001>
 Jan Forbrich  <https://orcid.org/0000-0001-8694-4966>
 Joe P. Ninan  <https://orcid.org/0000-0001-8720-5612>
 Oleg Kochukhov  <https://orcid.org/0000-0003-3061-4591>
 Vladimir S. Airapetian  <https://orcid.org/0000-0003-4452-0588>
 Sergio A. Dzib  <https://orcid.org/0000-0001-6010-6200>
 Charles J. Law  <https://orcid.org/0000-0003-1413-1776>
 Christian Rab  <https://orcid.org/0000-0003-1817-6576>

References

- Agresti, A. 2006, *An Introduction to Categorical Data Analysis* (New York: Wiley).
- Airapetian, V. S., Barnes, R., Cohen, O., et al. 2020, *IJAsB*, **19**, 136
- Airapetian, V., Meng, J., Junxiang, H., et al. 2023, *BAAS*, **55**, 005
- Alexander, F., & Preibisch, T. 2012, *A&A*, **539**, A64
- Alexander, R., Pascucci, I., Andrews, S., Armitage, P., & Cieza, L. 2014, in *Protostars and Planets VI*, ed. H. Beuther et al. (Tucson, AZ: Univ. Arizona Press), 475
- Alvarado-Gómez, J. D., Cohen, O., Drake, J. J., et al. 2022, *ApJ*, **928**, 147
- Argiroffi, C., Reale, F., Drake, J. J., et al. 2019, *NatAs*, **3**, 742
- Arnold, B. 1983, *Pareto Distributions, Statistical Distributions in Scientific Work Series* (Fairland, MD: International Co-operative Publishing House)
- Ayres, T. 2023, *AJ*, **166**, 212
- Baliunas, S. L., Donahue, R. A., Soon, W. H., et al. 1995, *ApJ*, **438**, 269
- Bressan, A., Marigo, P., Girardi, L., et al. 2012, *MNRAS*, **427**, 127
- Broos, P., Townsley, L., Getman, K., & Bauer, F. 2012, *AE: ACIS Extract, Astrophysics Source Code Library*, ascl:1203.001
- Broos, P. S., Townsley, L. K., Feigelson, E. D., et al. 2010, *ApJ*, **714**, 1582
- Brown, B. P., Oishi, J. S., Vasil, G. M., Lecoanet, D., & Burns, K. J. 2020, *ApJL*, **902**, L3
- Browning, M. K. 2008, *ApJ*, **676**, 1262
- Brunn, V., Rab, C., Marcowith, A., et al. 2024, *MNRAS*, **530**, 3669
- Caramazza, M., Flaccomio, E., Micela, G., et al. 2007, *A&A*, **471**, 645
- Carley, E. P., Vilmer, N., & Vourlidis, A. 2020, *FrASS*, **7**, 79
- Cash, W. 1979, *ApJ*, **228**, 939
- Chen, Y., Girardi, L., Bressan, A., et al. 2014, *MNRAS*, **444**, 2525
- Christensen, U. R., Holzwarth, V., & Reiners, A. 2009, *Natur*, **457**, 167
- Cleeves, L. I., Bergin, E. A., Öberg, K. I., et al. 2017, *ApJL*, **843**, L3
- Cody, A. M., Hillenbrand, L. A., & Rebull, L. M. 2022, *AJ*, **163**, 212
- Coffaro, M., Stelzer, B., & Orlando, S. 2022, *A&A*, **661**, A79
- Coffaro, M., Stelzer, B., Orlando, S., et al. 2020, *A&A*, **636**, A49
- Colombo, J. F., Caramazza, M., Flaccomio, E., Micela, G., & Sciortino, S. 2007, *A&A*, **474**, 495
- Da Rio, N., Tan, J. C., Covey, K. R., et al. 2016, *ApJ*, **818**, 59
- Davies, C. L., Gregory, S. G., & Greaves, J. S. 2014, *MNRAS*, **444**, 1157
- Emeriau-Viard, C., & Brun, A. S. 2017, *ApJ*, **846**, 8
- Ercolano, B., Picogna, G., Monsch, K., Drake, J. J., & Preibisch, T. 2021, *MNRAS*, **508**, 1675
- Espallat, C. C., Thanathibodee, T., Pittman, C. V., et al. 2023, *ApJL*, **958**, L4
- Favata, F., Flaccomio, E., Reale, F., et al. 2005, *ApJS*, **160**, 469
- Feigelson, E. D., Casanova, S., Montmerle, T., & Guibert, J. 1993, *ApJ*, **416**, 623
- Feigelson, E. D., Getman, K., Townsley, L., et al. 2005, *ApJS*, **160**, 379
- Flaccomio, E., Micela, G., Sciortino, S., et al. 2018, *A&A*, **620**, A55
- Forbrich, J., Dzib, S. A., Reid, M. J., & Menten, K. M. 2021, *ApJ*, **906**, 23
- Freeman, P., Doe, S., & Siemiginowska, A. 2001, *Proc. SPIE*, **4477**, 76
- Fruscione, A., McDowell, J. C., Allen, G. E., et al. 2006, *Proc. SPIE*, **6270**, 62701V
- Garmire, G. P., Bautz, M. W., Ford, P. G., Nousek, J. A., & Ricker, G. R. J. 2003, *Proc. SPIE*, **4851**, 28
- Garraffo, C., Drake, J. J., Dotter, A., et al. 2018, *ApJ*, **862**, 90
- Gehrels, N. 1986, *ApJ*, **303**, 336
- Getman, K. V., Broos, P. S., Kuhn, M. A., et al. 2017, *ApJS*, **229**, 28
- Getman, K. V., Broos, P. S., Salter, D. M., Garmire, G. P., & Hogerheijde, M. R. 2011, *ApJ*, **730**, 6
- Getman, K. V., & Feigelson, E. D. 2021, *ApJ*, **916**, 32
- Getman, K. V., Feigelson, E. D., Broos, P. S., Micela, G., & Garmire, G. P. 2008a, *ApJ*, **688**, 418
- Getman, K. V., Feigelson, E. D., Broos, P. S., Townsley, L. K., & Garmire, G. P. 2010, *ApJ*, **708**, 1760

- Getman, K. V., Feigelson, E. D., & Garmire, G. P. 2021, *ApJ*, **920**, 154
- Getman, K. V., Feigelson, E. D., & Garmire, G. P. 2023, *ApJ*, **952**, 63
- Getman, K. V., Feigelson, E. D., Garmire, G. P., et al. 2022, *ApJ*, **935**, 43
- Getman, K. V., Feigelson, E. D., Grosso, N., et al. 2005a, *ApJS*, **160**, 353
- Getman, K. V., Feigelson, E. D., Micela, G., et al. 2008b, *ApJ*, **688**, 437
- Getman, K. V., Flaccomio, E., Broos, P. S., et al. 2005b, *ApJS*, **160**, 319
- Glassgold, A. E., Feigelson, E. D., & Montmerle, T. 2000, in *Protostars and Planets IV*, ed. V. Mannings, A. P. Boss, & S. S. Russell (Tucson, AZ: Univ. Arizona Press), 429
- Glassgold, A. E., Najita, J. R., & Igea, J. 2007, *ApJ*, **656**, 515
- Gorti, U., & Hollenbach, D. 2009, *ApJ*, **690**, 1539
- Hazleton, M. L., & Marshall, J. C. 2009, *Statistics & Probability Letters*, **79**, 999
- Hazra, G., Vidotto, A. A., Carolan, S., Villarreal D'Angelo, C., & Manchester, W. 2022, *MNRAS*, **509**, 5858
- He, X., & Ng, P. 1999, *Computational Statistics*, **14**, 315
- Ibañez Bustos, R. V., Buccino, A. P., Flores, M., & Mauas, P. J. D. 2019, *A&A*, **628**, L1
- Ibañez Bustos, R. V., Buccino, A. P., Messina, S., Lanza, A. F., & Mauas, P. J. D. 2020, *A&A*, **644**, A2
- Irving, Z. A., Saar, S. H., Wargelin, B. J., & do Nascimento, J.-D. 2023, *ApJ*, **949**, 51
- Judge, P. G., Saar, S. H., Carlsson, M., & Ayres, T. R. 2004, *ApJ*, **609**, 392
- Käpylä, P. J. 2021, *A&A*, **651**, A66
- Käpylä, P. J., Browning, M. K., Brun, A. S., Guerrero, G., & Warnecke, J. 2023, *SSRv*, **219**, 58
- Kirichenko, A. S., & Bogachev, S. A. 2017, *SoPh*, **292**, 120
- Kochukhov, O. 2021, *A&ARv*, **29**, 1
- Kochukhov, O., Hackman, T., Lehtinen, J. J., & Wehrhahn, A. 2020, *A&A*, **635**, A142
- Kounkel, M., Covey, K., Moe, M., et al. 2019, *AJ*, **157**, 196
- Kuhn, M. A., Getman, K. V., Broos, P. S., Townsley, L. K., & Feigelson, E. D. 2013, *ApJS*, **209**, 27
- Legendre, P., & Legendre, L. 1998, *Numerical Ecology*, Developments in Environmental Modelling No. 20 (2nd ed.; Amsterdam: Elsevier)
- Matt, S. P., Brun, A. S., Baraffe, I., Bouvier, J., & Chabrier, G. 2015, *ApJL*, **799**, L23
- Megeath, S. T., Gutermuth, R., Muzerolle, J., et al. 2012, *AJ*, **144**, 192
- Moschou, S.-P., Drake, J. J., Cohen, O., et al. 2019, *ApJ*, **877**, 105
- Namekata, K., Airapetian, V. S., Petit, P., et al. 2024, *ApJ*, **961**, 23
- Namekata, K., Maehara, H., Honda, S., et al. 2021, *NatAs*, **6**, 241
- Nasa High Energy Astrophysics Science Archive Research Center (Heasarc), 2014, HEASoft: Unified Release of FTOOLS and XANADU, Astrophysics Source Code Library, ascl:1408.004
- Ng, P. T., & Maechler, M. 2007, *Statistical Modelling*, **7**, 315
- Orlando, S., Favata, F., Micela, G., et al. 2017, *A&A*, **605**, A19
- Owen, J. E. 2019, *AREPS*, **47**, 67
- Pevtsov, A. A., Fisher, G. H., Acton, L. W., et al. 2003, *ApJ*, **598**, 1387
- Preibisch, T., Kim, Y.-C., Favata, F., et al. 2005, *ApJS*, **160**, 401
- Rab, C., Güdel, M., Padovani, M., et al. 2017, *A&A*, **603**, A96
- R Core Team 2020, R: A Language and Environment for Statistical Computing, R Foundation for Statistical Computing, Vienna, Austria, <https://www.R-project.org>
- Reiners, A., Basri, G., & Christensen, U. R. 2009, *ApJ*, **697**, 373
- Reiners, A., & Christensen, U. R. 2010, *A&A*, **522**, A13
- Reiners, A., Shulyak, D., Käpylä, P. J., et al. 2022, *A&A*, **662**, A41
- Richert, A. J. W., Getman, K. V., Feigelson, E. D., et al. 2018, *MNRAS*, **477**, 5191
- Robrade, J., Schmitt, J. H. M. M., & Favata, F. 2012, *A&A*, **543**, A84
- Sanz-Forcada, J., Stelzer, B., Coffaro, M., Raetz, S., & Alvarado-Gómez, J. D. 2019, *A&A*, **631**, A45
- Scargle, J. D. 1998, *ApJ*, **504**, 405
- Scargle, J. D., Norris, J. P., Jackson, B., & Chiang, J. 2013, *ApJ*, **764**, 167
- Siess, L., Dufour, E., & Forestini, M. 2000, *A&A*, **358**, 593
- Skiff, B. A. 2014, *yCat*, **B/mk**
- Sokal, K. R., Johns-Krull, C. M., Mace, G. N., et al. 2020, *ApJ*, **888**, 116
- Stelzer, B., Flaccomio, E., Briggs, K., et al. 2007, *A&A*, **468**, 463
- Stelzer, B., Flaccomio, E., Montmerle, T., et al. 2005, *ApJS*, **160**, 557
- Telleschi, A., Güdel, M., Briggs, K. R., Audard, M., & Palla, F. 2007, *A&A*, **468**, 425
- Terrien, R. C., Keen, A., Oda, K., et al. 2022, *ApJL*, **927**, L11
- Townsley, L. K., Broos, P. S., Garmire, G. P., & Povich, M. S. 2019, *ApJS*, **244**, 28
- Townsley, L. K., Broos, P. S., Garmire, G. P., et al. 2014, *ApJS*, **213**, 1
- Voronig, A. M., Odert, P., Leitzinger, M., et al. 2021, *NatAs*, **5**, 697
- Villadsen, J., & Hallinan, G. 2019, *ApJ*, **871**, 214
- Waggoner, A. R., & Cleeves, L. I. 2022, *ApJ*, **928**, 46
- Waggoner, A. R., Cleeves, L. I., Loomis, R. A., et al. 2023, *ApJ*, **956**, 103
- Wand, M. P., & Jones, M. C. 1994, *Kernel Smoothing* (New York: Chapman and Hall/CRC)
- Wargelin, B. J., Saar, S. H., Pojmański, G., Drake, J. J., & Kashyap, V. L. 2017, *MNRAS*, **464**, 3281
- Warton, D. I., Wright, I. J., Falster, D. S., & Westoby, M. 2006, *BioRv*, **81**, 259
- Washinoue, H., Takasao, S., & Furuya, K. 2024, arXiv:2406.04946
- Weisskopf, M. C., Brinkman, B., Canizares, C., et al. 2002, *PASP*, **114**, 1
- Woitke, P., Thi, W. F., Arabhavi, A. M., et al. 2024, *A&A*, **683**, A219
- Wolk, S. J., Hamden, F. R. J., Flaccomio, E., et al. 2005, *ApJS*, **160**, 423
- Yadav, R. K., Christensen, U. R., Wolk, S. J., & Poppenhaeger, K. 2016, *ApJL*, **833**, L28
- Zhuleku, J., Warnecke, J., & Peter, H. 2021, arXiv:2102.00982